Simultaneous Measurements of Velocity and Temperature in the Heated Wake of a Cylinder with Applications to the Modeling of Turbulent Passive Scalars

Arpi Berajeklian

Supervised by Professor Laurent Mydlarski

Department of Mechanical Engineering
McGill University

A thesis submitted to McGill University in partial fulfillment of the requirements for the degree of Master of Engineering

© Arpi Berajeklian, Montreal, Canada, June 2010

Abstract

The present work focuses on the mixing of passive scalars in a turbulent flow (i.e., scalars that do not disturb the velocity field in which they are transported). To this end, small temperature differences are mixed in a turbulent air flow. Of particular interest are (i) the turbulent Prandtl number (Pr_T), and (ii) the mechanical-to-thermal time-scale ratio (r) – two recurring quantities employed by modellers, determined from experiments, and generally assumed to be constant based on the type of flow. The objective of the work is to study the sensitivity of these two quantities to differences in their injection method within the same flow. To achieve this goal, mixed velocity-temperature statistics were measured in the wake of a circular cylinder. The wake was heated by one of two ways: heating the cylinder, or heating an array of fine parallel wires (called a mandoline) placed downstream of the cylinder.

The experimental results demonstrate that the magnitude of Pr_T varies throughout the wake for both scalar fields and is consistently greater than the typical value of 0.7 used in turbulence models. Furthermore, Pr_T differs for the two scalar injection methods, despite being within the same flow. Likewise, the values of r vary across the wake for both scalar fields and significant differences exist between the two scalar injection methods. Hence, both Pr_T and r not only depend on the type of flow, but on the scalar field injection mechanism method as well. This dependence should be taken into account in turbulence models.

Résumé

Ce travail est une étude du mélange de scalaires passifs en écoulements turbulents. (Un scalaire est dit passif s'il n'exerce pas d'influence sur le champ de vitesse qui le transporte). Par exemple, nous considérons de faibles différences de température mélangées sont considérées au sein d'un écoulement turbulent d'air comme le scalaire passif. Nous sommes particulièrement intéressés par i) le nombre de Prandtl turbulent (Pr_T) et ii) le rapport d'échelle des temps dynamique et thermique (r) – deux quantités utilisées pour la modélisation de scalaires passifs en écoulements turbulents. Ces deux quantités sont généralement considérées comme des constantes et déterminées à partir de résultats expérimentaux. L'objectif de cette thèse est d'étudier la sensibilité de ces deux quantités aux différentes méthodes d'injection dans l'écoulement turbulent. Pour atteindre cet objectif, nous réalisons des mesures simultanées de vitesse et de température dans le sillage d'un cylindre. Ce sillage peut être chauffé de deux façons différentes: soit le cylindre lui-même est chauffé, ou une mandoline placée en aval du cylindre est chauffée.

Les résultats expérimentaux démontrent que Pr_T varie pour les deux méthodes d'injection du scalaire, bien que le champ dynamique demeure identique dans les deux cas. D'autre part, les valeurs mesurées sont systématiquement plus grandes que la valeur typique de 0.7 utilisée en modélisation. De plus, r varie lui aussi à travers le sillage pour les deux types d'injection utilisés. Ainsi, nous observons que Pr_T et r sont à la fois dépendants du champ dynamique et du type d'injection utilisé. Cette dernière dépendance devrait être aussi considérée dans les modèles de turbulence.

Acknowledgments

To start, I would like to thank Professor Mydlarski for being a great supervisor, teacher, and advisor during the course of my work. I appreciate how he generously helped me with my thesis and how he always found time for meetings. During my time working in his team, I learned a great deal about performing experiments, working independently, and thinking thoroughly and critically. For that, I am extremely thankful.

I would like to thank the turbulence team, especially: Jason Lepore, for helping with the experimental work and editing my thesis; Emmanuel Germaine, for helping me translate my abstract into French; and Samer Afara, for motivating me to constantly think critically.

A special thanks is extended to Georges Tewfik and Mario Iacobaccio from the measurement lab for helping with the electrical components of my experimental setup. Additionally, I would like to extend my thanks to Tara Mawhinney, the liaison librarian from the Schulich library, for enthusiastically helping me locate hard-to-find references.

I am grateful for my family and friends who provided me with support and encouragement throughout my work; most importantly, Jeffrey Poissant who believed in me, helped me with the experimental setup, and edited my thesis.

Finally, my appreciation and thanks are extended to the Natural Science and Engineering Research Council of Canada (NSERC) for funding my research during the 2008-2010 period.

Table of Contents

List of Figures

List of Tables

Nomenclature

Roman

a	Power law constant for the decay of the velocity fluctuations
A	Hot-wire calibration constant and Gaussian curve constant
$\overline{A}$	Calibration constant for non-isothermal flows
AD	Symbolic notation to represent the instantaneous advection-diffusion equations
$\overline{AD}$	Symbolic notation to represent the Reynolds-averaged advection-diffusion equations
b	Power law constant for the decay of the scalar fluctuations
B	Hot-wire calibration constant and Gaussian curve constant
$\overline{B}$	Calibration constant for non-isothermal flows
C	Cold-wire calibration constant
c_1, c_2, c_3, c_4	Constants of the mean temperature excess curve-fit
C_1, C_2, C_3	Constants of the cold-wire response equation
c_θ	Numerical constant in a turbulence model for passive scalars
D	Cold-wire calibration constant and cylinder or nozzle diameter
d_{wire}	Wire diameter of the mandoline
d_{ij}	Diffusivity tensor
E	Output voltage of the CTA or CCA
E_1, E_2	Output voltage of the CTA for each hot-wire on the X-probe
E_{DAQ}	Voltage span at which data is acquired by the DAQ board
$E_q(f)$	Power spectrum of a variable q
f	Frequency
f_c	Cut-off frequency of the cold-wire
$f_c^{'}$	Low-pass frequency
f_m	Resonance frequency of the mandoline wires

f_v	Vortex shedding frequency
g_i	Gravitational acceleration
h	Velocity half-width
$H_f(f)$	Filter function used for the compensation of the cold-wire signal
$\left\|H_f(f)\right\|$	Filter gain used for the compensation of the cold-wire signal
k	Turbulent kinetic energy and longitudinal cooling constant for a hot-wire
k_θ	Scalar variance $(\equiv \overline{\theta^2}/2)$
K_q	Kurtosis of a variable q
ℓ	Integral length scale of the velocity field
ℓ_θ	Integral length scale of the thermal field
l_w	Length of the cold-wire and the mandoline wire
L	Length of the cylinder
n	Decay exponent for the velocity fluctuations and hot-wire calibration constant
N	Number of data points
NS	Symbolic notation to represent the instantaneous Navier-Stokes equations
$\overline{NS}$	Symbolic notation to represent the Reynolds-averaged Navier-Stokes equations
m	Decay exponent for the temperature fluctuations
M	Grid mesh length
M_θ	Mandoline wire spacing
$\widetilde{P}$	Instantaneous pressure
$\overline{P}$	Mean pressure
Pe_T	Turbulent Péclet number
Pr	Prandtl number
Pr_T	Turbulent Prandtl number
q_{RMS}	Root mean square (RMS) of the variable q

r	Mechanical-to-thermal time-scale ratio
r_{av}	Spatially averaged mechanical-to-thermal time-scale ratio
Re_D	Reynolds number based on the cylinder's or round jet's diameter
$\mathrm{Re}_{d_{wire}}$	Reynolds number based on the mandoline's wire diameter
s_{ij}	Fluctuating strain-rate
S	Instantaneous velocity experienced by the two inclined hot-wires
S_t	Strouhal number
S_q	Skewness of the variable q
t	Time
$\overline{T}$	Mean temperature
T_{film}	Film temperature
$T_{w,a}$, $T_{w,b}$	X-probe calibration constants
T_{wire}	Temperature of the mandoline wire
T_∞	Free-stream temperature
$\Delta\overline{T}$	Mean temperature excess
U_1, U_2	Velocities corresponding to the output voltages, E_1 and E_2, from each hot-wire
U_c	Centerline velocity
U_{eff}	Effective velocity
$\widetilde{U}_i$	Instantaneous velocity
$\overline{U}_i$	Mean velocity
U_∞	Free-stream velocity
u, v, w	Velocity fluctuations in the x-, y-, and z- directions, respectively
W	Mandoline width
x, y, z	Cartesian coordinates
y_o / D	Offset constant used for curve-fitting the mean velocity and temperature profiles

Greek

α	Scalar or thermal molecular diffusivity in the fluid
α_T	Turbulent thermal diffusivity
β	Angle from the mean flow direction cooling the hot-wires
$\frac{\delta q}{q}$	Relative uncertainty of the variable q
ε	Dissipation rate of the turbulent kinetic energy
ε_θ	Dissipation rate of scalar variance
η	Kolmogorov microscale for the velocity field
η_θ	Kolmogorov microscale for the scalar field
θ	Temperature fluctuation
θ_{eff}	Effective angle
θ_1, θ_2	Effective angle of each hot-wire
$\widetilde{\Theta}$	Instantaneous scalar (concentration or temperature)
ν	Kinematic viscosity of the fluid
ν_T	Turbulent viscosity
ρ	Density of the fluid
σ	Standard deviation of a Gaussian profile
σ_A	Standard uncertainty of the hot-wire calibration constant A
σ_B	Standard uncertainty of the hot-wire calibration constant B
τ	Integral time-scale of turbulence
τ_E	Time constant of the electronics of the constant current anemometer
τ_w	Time constant of the cold-wire
$\phi(f)$	Phase of the filter function for the compensation of the cold-wire signal

Chapter 1: Background and Motivation

1.1 Introduction

Fluid mechanics plays a fundamental role in many aspects of engineering. It encompasses a large variety of engineering applications, such as fluid flow over vehicles, piping systems, and energy generation (e.g., windmills, turbines, etc). Furthermore, the majority of engineering flows are turbulent: boundary layers on airplane wings, many combustion processes, most flows in pipelines, etc. One remarkable aspect of turbulence is its ability to mix mass, momentum, and energy rapidly, and more effectively than in a process that occurs solely by molecular interactions (as is the case in laminar flows). Therefore, having a thorough understanding of turbulence is important to accurately predict and efficiently implement the variety of flows encountered in engineering — a challenging objective given the non-linear and chaotic nature of turbulent flows.

To demonstrate this challenge, consider the contrast between laminar and turbulent flow predictions. In laminar flows, one can obtain analytical or semi-analytical results for the simplest cases (e.g., Poiseuille flow in a smooth pipe, or Blasius' similarity solution for flow over a flat plate of a Newtonian, constant property fluid). More complicated laminar flows can be predicted by discretizing the domain of interest and solving the Navier-Stokes equations computationally. Turbulence, on the other hand, is so complex that even for the simplest flows (e.g., homogenous, isotropic turbulence) there are no analytical solutions to the

instantaneous Navier-Stokes equations. Furthermore, a complete numerical solution of turbulent flows is beyond the capabilities of modern computers, because, for typical engineering flows, simulation of all the inherent length and time scales requires vast computational resources. Therefore, engineers usually rely either on empirical correlations to predict time-averaged quantities, or must make reasonable approximations to simplify the governing equations (i.e., turbulence models). The latter approach, herein referred to as *modeling*, is more versatile, but requires a thorough understanding of the fundamentals of turbulence.

Although it is difficult to provide a complete and precise definition of turbulence, its characteristics are well known: turbulent flows are random, possess large diffusivities, occur at large Reynolds numbers, contain a wide range of length and time scales, exhibit three-dimensional vorticity fluctuations, and are dissipative. Since turbulence consists of random fluctuations of quantities (such as fluid velocity) and occurs over a range of time and length scales, two types of mathematical tools are frequently used for its study: (i) statistical and (ii) spectral tools. The former deals with probabilistic techniques relating to fluctuating quantities, and the latter describes the distribution of a given quantity over ranges of length and/or time scales. Some turbulence models are based on statistical tools and others on spectral tools.

Accurately modeling turbulence is difficult, as previously mentioned; certain models often work well for only a few types of flows. To validate and guide the formulation of these models, turbulence researchers often rely on experimental results. Thus, performing rigorous experiments to uncover the underlying mechanisms of turbulent flows is a critical component of turbulence research.

One interesting branch of turbulence is the study of scalar mixing in turbulent flows. A scalar can be temperature, pollutant or any other chemical species within a turbulent flow. Scalar mixing has applications to heat transfer, combustion, meteorology, environmental pollutant dispersion, etc. A particular interest is given to the study of *passive* scalar mixing in turbulent flows, the simplest, yet still unsolved case of scalar mixing. A passive scalar is one that does not disturb the velocity field in which it is injected. Temperature is, for example, considered to be a passive scalar when the range of temperature differences in a flow is small, rendering buoyancy effects negligible.

1.2 Theoretical Background on Modeling of Passive Scalars in Turbulent Flows

Turbulent flows are described by the governing equations of fluid mechanics. The assumptions used herein are: a Newtonian, constant property fluid. Hence, the instantaneous continuity and Navier-Stokes equations describing turbulent flows in Cartesian coordinates are (noting that a tilde is used to denote instantaneous variables):

$$\frac{\partial \widetilde{U}_i}{\partial x_i} = 0 \text{, and} \tag{1.1}$$

$$\frac{\partial \widetilde{U}_i}{\partial t} + \widetilde{U}_j \frac{\partial \widetilde{U}_i}{\partial x_j} = -\frac{1}{\rho}\frac{\partial \widetilde{P}}{\partial x_i} + \nu \frac{\partial^2 \widetilde{U}_i}{\partial x_j \partial x_j}, \tag{1.2}$$

respectively. The instantaneous advection-diffusion equation for a passive scalar is:

$$\frac{\partial \widetilde{\Theta}}{\partial t} + \widetilde{U}_i \frac{\partial \widetilde{\Theta}}{\partial x_i} = \alpha \frac{\partial^2 \widetilde{\Theta}}{\partial x_i \partial x_i}. \tag{1.3}$$

$\widetilde{U}_i$ is the instantaneous velocity, $\widetilde{P}$ is the instantaneous pressure, $\widetilde{\Theta}$ is the instantaneous scalar (which could be a small temperature excess or concentration of a chemical species), ρ is the density of the fluid, ν is the kinematic viscosity of the fluid, and α is the scalar's molecular diffusivity in the given fluid.

Many techniques in computational fluid dynamics are used to approximate the solution to these coupled, non-linear partial differential equations. (i) Direct Numerical Simulation (DNS) solves the instantaneous governing equations and hence resolves all the scales of the turbulent flow. However, the computational cost is high because the domain requires an extremely high resolution to capture the smallest scales of typical turbulent flows. (ii) Large Eddy Simulation (LES) resolves the large-eddies of the flow. "Filtered" governing equations, which describe the large-eddies and contain an extra term that incorporates the effect of the small-eddies, are solved. LES is computationally less expensive than DNS; however, in wall-bounded flows, the small scales (not captured by LES) play a critical role in describing the dynamics of the near-wall regions. Thus, this challenge can limit certain applications. (iii) Reynolds-Averaged Navier-Stokes (RANS) methods solve the Reynolds-averaged governing equations (described in section 1.2.1). These methods are the least computationally intensive and provide practical quantities for engineering applications. Thus, RANS models are widely used in industry and are the focus of the next sub-sections (1.2.1 and 1.2.2). These sub-sections will describe the different approaches used to predict turbulent passive scalars and highlight the parameters to be considered in this work.

1.2.1 Solving for the Mean Scalar Field

Since turbulent flows are chaotic in nature, understanding their behaviour becomes challenging should the instantaneous variables be solely observed. Therefore, it is customary to decompose instantaneous variables into the sum of their average (mean) component and a fluctuating (turbulent) component. (This is called the Reynolds decomposition.) For example, the instantaneous longitudinal velocity, $\widetilde{U}$, is split into the sum of the mean velocity, $\overline{U}$ (denoted by an overbar), and the velocity fluctuation, u, giving $\widetilde{U} = \overline{U} + u$. Once all the instantaneous terms in the governing equations are replaced by this decomposition, each term is then averaged. Noting that, by definition, the average of the fluctuation is zero (e.g., $\overline{u} = 0$), the Reynolds-averaged continuity and Navier-Stokes equations become:

$$\frac{\partial \overline{U}_i}{\partial x_i} = 0\,, \tag{1.4}$$

$$\frac{\partial \overline{U}_i}{\partial t} + \overline{U}_j \frac{\partial \overline{U}_i}{\partial x_j} = -\frac{1}{\rho}\frac{\partial \overline{P}}{\partial x_i} + \frac{\partial}{\partial x_j}\left(\nu \frac{\partial \overline{U}_i}{\partial x_j} - \overline{u_i u_j}\right). \tag{1.5}$$

The new quantities $\overline{u_i u_j}$, called the Reynolds stresses, are generated by the non-linear advection term and represent the transport of momentum by the turbulent velocity fluctuations. The Reynolds stresses give rise to what is known as the closure problem (i.e., more unknowns than equations). Additional relationships are therefore necessary to solve for all the unknowns.

Similarly, this procedure is applied to passive scalars, resulting in the Reynolds-averaged advection-diffusion equation:

$$\frac{\partial \overline{\Theta}}{\partial t} + \overline{U_i}\frac{\partial \overline{\Theta}}{\partial x_i} = \frac{\partial}{\partial x_i}\left(\alpha \frac{\partial \overline{\Theta}}{\partial x_i} - \overline{u_i \theta}\right). \tag{1.6}$$

The new quantities $\overline{u_i \theta}$, called the turbulent scalar fluxes, are generated by the advection term and represent the transport of the scalar fluctuations by the turbulent velocity fluctuations. Again, the closure problem appears even if the velocity field is known, and additional relationships are needed to model $\overline{u_i \theta}$ and close the Reynolds-averaged advection-diffusion equation. There are two main approaches to solve for $\overline{u_i \theta}$: (i) using the gradient transport hypothesis (sub-section 1.2.1.1), and (ii) modeling the turbulent flux budget (sub-section 1.2.1.2).

1.2.1.1 Modeling the Turbulent Flux using the Gradient Transport Hypothesis

Gradient transport models are often used in turbulence modeling to close the Reynolds-averaged governing equations. Physically, the gradient transport hypothesis assumes that mass, momentum, and energy exchange, resulting from turbulent eddies, can be modeled like colliding molecules in laminar flows. In other words, it is assumed that there is a linear relationship between the turbulent fluxes and the gradient of a mean quantity. Such models are based on analogies with molecular transport relationships, such as the stress and strain-rate relationships for Newtonian fluids, Fourier's law for conduction, or Fick's law for diffusion. For example, the gradient transport hypothesis relates the Reynolds stress to the mean velocity as follows:

$$-\rho \overline{u_i u_j} = \rho \nu_T \left(\frac{\partial \overline{U_i}}{\partial x_j} + \frac{\partial \overline{U_j}}{\partial x_i}\right) - \frac{1}{3}\rho \overline{u_k u_k}\delta_{ij}, \tag{1.7}$$

where ν_T is the so-called "turbulent viscosity." Much like its molecular counterpart, the kinematic viscosity (ν), which describes how momentum is exchanged between colliding molecules, the turbulent viscosity describes the exchange of momentum by turbulent eddies. However, unlike ν, which is a property of the fluid, ν_T is a property of the flow (i.e., it depends on the characteristics of the turbulence, and can vary across the flow).

Similarly, for the passive scalar field (where the passive scalar used herein is temperature, hence $\overline{\Theta}$ is replaced by $\overline{T}$), the turbulent heat flux is related to the mean temperature as follows:

$$\overline{u_i\theta} = -\alpha_T \frac{\partial \overline{T}}{\partial x_i}, \tag{1.8}$$

where α_T is the "turbulent thermal diffusivity." Whereas the (molecular) thermal diffusivity (α) relates to the exchange of internal energy between molecules, the turbulent thermal diffusivity (α_T) describes the exchange of internal energy due to turbulent eddies.

Continuing to draw inspiration from molecular interactions, a *turbulent* Prandtl number can be defined. The turbulent Prandtl number relates how fast turbulence transports momentum compared to internal energy. Therefore, the turbulent Prandtl number is defined as follows:

$$\mathrm{Pr}_T \equiv \frac{\nu_T}{\alpha_T}. \tag{1.9}$$

The Reynolds-averaged advection-diffusion is then typically closed by expressing the turbulent flux as a function of ν_T and Pr_T:

$$\overline{u_i\theta} = -\alpha_T \frac{\partial \overline{T}}{\partial x_i} = -\left(\frac{\nu_T}{\mathrm{Pr}_T}\right)\frac{\partial \overline{T}}{\partial x_i}. \tag{1.10}$$

This relationship is often used because Pr_T is usually assumed to be constant throughout the flow. Using this assumption simplifies the computational work required to predict the scalar field; the only extra unknown is ν_T which can be determined when solving for the velocity field by using algebraic (e.g., Prandtl's mixing length), one-equation (e.g., turbulent kinetic energy equation) or two-equation (e.g., $k-\varepsilon$ equations) turbulence models.

Despite being conceptually simple, gradient transport models have disadvantages. The gradient transport hypothesis assumes that the turbulent flux vector and the gradient vector of the mean quantity are related to each other by a scalar (i.e, ν_T and α_T are scalars). This assumption implies that these two vectors are aligned. However, many observations have contradicted this assumption. For example, it has been found that (i) counter-gradient transport (where ν_T or α_T are negative) (Bunker, 1956), or (ii) cases where the two vectors are misaligned (Tavoularis and Corrsin, 1981), can occur. To overcome this limitation the turbulent diffusivity (e.g. ν_T or α_T) is replaced by a more general expression – the diffusivity tensor, d_{ij}. However, even with d_{ij}, cases exist where the mean gradient is zero but the turbulent flux is not (Warhaft, 1980). Furthermore, this hypothesis is based on the idea that the characteristic time scale of the turbulent eddies is on the same order of magnitude as the characteristic time scale of the mean flow. Consequently, this means that gradient transport models are capable of describing turbulent flows which are characterized by only one velocity scale and one length scale.

1.2.1.2 Modeling of the Turbulent Heat Flux Transport Equations

Instead of using gradient transport relationships to solve for $\overline{u_i\theta}$, a turbulent heat flux transport equation can be derived and individual terms in the equation are then modeled. To derive such an equation, the instantaneous Navier-Stokes (denoted by *NS*) and the Reynolds-averaged Navier-Stokes ($\overline{NS}$) equations are used as well as the instantaneous advection-diffusion (*AD*) and the Reynolds-averaged advection-diffusion ($\overline{AD}$). The following equation is calculated (using the symbolic notation described above):

$$\theta\left(NS-\overline{NS}\right)+u_i\left(AD-\overline{AD}\right), \tag{1.11}$$

where $\left(NS-\overline{NS}\right)$ is multiplied by the scalar fluctuation and $\left(AD-\overline{AD}\right)$is multiplied by the velocity fluctuation. Then $\theta\left(NS-\overline{NS}\right)+u_i\left(AD-\overline{AD}\right)$ is averaged and simplified to become the turbulent heat flux budget:

$$\begin{aligned}\underbrace{\frac{\partial\overline{u_i\theta}}{\partial t}+\overline{U_j}\frac{\partial\overline{u_i\theta}}{\partial x_j}}_{\text{(a)}} &= \underbrace{-\frac{\partial\left(\overline{u_iu_j\theta}\right)}{\partial x_j}}_{\text{(b)}}\underbrace{-\frac{1}{\rho}\frac{\partial\overline{\theta p}}{\partial x_i}}_{\text{(c)}}+\underbrace{\frac{\partial}{\partial x_j}\left(\nu\theta\overline{\frac{\partial u_i}{\partial x_j}}+\alpha\overline{u_i\frac{\partial\theta}{\partial x_j}}\right)}_{\text{(d)}}\\ &\underbrace{-\overline{u_iu_j}\frac{\partial\overline{\mathrm{T}}}{\partial x_j}}_{\text{(e)}}\underbrace{-\overline{u_j\theta}\frac{\partial\overline{U_i}}{\partial x_j}}_{\text{(f)}}+\underbrace{\frac{1}{\rho}\overline{p\frac{\partial\theta}{\partial x_i}}}_{\text{(g)}}\underbrace{-(\nu+\alpha)\overline{\frac{\partial u_i}{\partial x_j}\frac{\partial\theta}{\partial x_j}}}_{\text{(h)}}.\end{aligned} \tag{1.12}$$

The table below gives an interpretation of each term of the turbulent heat flux budget:

	Term	Interpretation of the terms
Material derivative	(a)	time derivative and spatial convective derivative
Transport terms	(b)	transport of $\overline{u_i\theta}$ due to turbulent velocity fluctuations
	(c)	transport of $\overline{u_i\theta}$ due to turbulent pressure fluctuations
	(d)	molecular transport of $\overline{u_i\theta}$
Source and sink terms	(e)	production of $\overline{u_i\theta}$ due to mean temperature gradients
	(f)	production of $\overline{u_i\theta}$ due to mean velocity gradients
	(g)	redistribution term in the balance of $\overline{u_i\theta}$
	(h)	molecular "dissipation" term

Table 1.1: Interpretation of the terms of the turbulent heat flux budget

After deriving the turbulent heat flux budget, new unknowns appear: $\overline{u_i u_j \theta}$, $\overline{\theta p}$, $\overline{p\frac{\partial \theta}{\partial x_i}}$, $\overline{\frac{\partial u_i}{\partial x_j}\frac{\partial \theta}{\partial x_j}}$, $\overline{\theta\frac{\partial u_i}{\partial x_j}}$, and $\overline{u_i\frac{\partial \theta}{\partial x_j}}$, again indicating the persistence of the closure problem. The goal is to model terms (b), (c), (d), (g), and (h) as functions of the "known" quantities which already appear in terms (a), (e), and (f) to close this system of equations. These "known" quantities include $\overline{U_i}$, $\overline{p}$, $\overline{u_i u_j}$, $\overline{T}$, $\overline{u_i\theta}$, and others to be discussed. *Modeling and Simulation of Turbulent Flows* by Schiestel (2008) provides a concise explanation of how each term is modeled by various turbulence modellers. Thus the remainder of this section will highlight the key points from this book on how each term is modeled. Although not presented in Schiestel, note that the gradient transport hypothesis could be used to model the terms as well.

Terms (c), (d), and (h) can be neglected by performing an order of magnitude analysis and assuming that the turbulent Reynolds number is high and that the Prandtl number remains near unity. Hence, only terms (b) and (g) need to be modeled. For term (b), the triple correlation, $\overline{u_i u_j \theta}$, is modeled by looking at its transport equation (which is derived in a similar manner as the transport equation for $\overline{u_i\theta}$:

$$\frac{D\overline{u_i u_j \theta}}{Dt} = -\overline{u_i u_k \theta}\frac{\partial \overline{U_j}}{\partial x_k} - \overline{u_k u_j \theta}\frac{\partial \overline{U_i}}{\partial x_k} - \overline{u_i u_j u_k}\frac{\partial \overline{T}}{\partial x_k} - \frac{\partial \overline{u_i u_j u_k \theta}}{\partial x_k} - \frac{1}{\rho}\left(\overline{u_i \theta \frac{\partial p}{\partial x_j}} + \overline{u_j \theta \frac{\partial p}{\partial x_i}}\right)$$

$$+ \overline{u_i \theta}\frac{\partial \overline{u_j u_k}}{\partial x_k} + \overline{u_i u_j}\frac{\partial \overline{u_k \theta}}{\partial x_k} + \overline{u_j \theta}\frac{\partial \overline{u_i u_k}}{\partial x_k}. \tag{1.13}$$

Having derived the transport equations for $\overline{u_i u_j \theta}$, additional unknowns are introduced; these also have to be modeled. For the sake of brevity, the details of modeling these terms are not described herein. Once all terms are modeled, $\overline{u_i u_j \theta}$ is expressed as a function of the following terms:

$$\overline{u_i u_j \theta} = \Im\left(\overline{u_i u_j}, \overline{u_i \theta}, \frac{k}{\varepsilon}, c_\theta\right). \tag{1.14}$$

k is the turbulent kinetic energy and is defined as:

$$k \equiv \frac{\overline{u_i u_i}}{2}. \tag{1.15}$$

It is the average (turbulent) kinetic energy per unit mass of the turbulent fluctuations. k is an important quantity in the study of turbulence: (i) it is related to the largest velocity scales of turbulence, (ii) it helps describe the dynamics of the velocity fluctuations, and (iii) it is widely used in turbulence modeling to predict the mean velocity field. ε is the dissipation rate of k (i.e., the rate at which k is converted into internal energy):

$$\varepsilon \equiv 2\nu \overline{s_{ij} s_{ij}}, \tag{1.16}$$

where s_{ij} is the fluctuating strain-rate, $s_{ij} \equiv \frac{1}{2}\left(\frac{\partial u_i}{\partial x_j} + \frac{\partial u_j}{\partial x_i}\right)$. ε is also an important quantity in the study of turbulence: (i) along with the kinematic viscosity, it can quantify the small scales, (ii) along with k, it is related to the integral time-scale of

turbulence, $\tau\ (\equiv k/\varepsilon)$, and (iii) it is also widely used in turbulence modeling to predict the mean velocity field (k-ε models). Finally, c_θ is a constant determined from "numerical optimization" (meaning that the numerical data is fitted to experimental measurements).

Having modeled term (b), only term (g) remains. Despite the importance of term (g), the derivation describing how to model this term is complicated and is not critical to this work (for more information, refer to Schiestel, 2008). This derivation involves taking the divergence of the fluctuating velocity equation, which simplifies to the Poisson equation, which is then solved using Green's functions. Multiplying the solution by $\frac{\partial\theta}{\partial x_i}$ and averaging gives an expression for term (g) as a function of several new unknowns. Modeling these unknowns allows term (g) to be presented in three parts: (i) a non-linear term, (ii) a linear term, and (iii) a near-wall term (this last term is neglected when far from a wall). Finally, term (g) takes on the following functional form:

$$\frac{1}{\rho}\overline{p\frac{\partial\theta}{\partial x_i}} = \underbrace{\Im\left(\overline{u_i u_j}, \overline{u_i\theta}, \frac{k}{\varepsilon}, c_{\theta\, non-linear}\right)}_{\text{non-linear term}} + \underbrace{\Im\left(\overline{U_i}, \overline{u_i\theta}, c_{\theta\, linear}\right)}_{\text{linear term}} + \underbrace{\Im\left(\overline{U_i}, \overline{u_i\theta}, \frac{k}{\varepsilon}, c_{\theta\, near-wall}\right)}_{\text{near-wall term}} \tag{1.17}$$

Various approximations for each term have been presented in the literature and typically consist of an equation with one or two numerical constants. By examining simple turbulent flows, the turbulent heat flux budgets are simplified to determine these numerical constants, which end up being expressed as functions of the turbulent Prandtl number (Pr_T) and other measurable quantities. Using

experimental results from the literature, the numerical constants can be determined and are assumed to be constant throughout the flow (but may have a different value depending on the type of flow).

Therefore, the modeled form of the turbulent heat flux budget becomes:

$$\underbrace{\frac{\partial \overline{u_i\theta}}{\partial t}+\overline{U_j}\frac{\partial \overline{u_i\theta}}{\partial x_j}}_{\text{(a)}}=\underbrace{-\frac{\partial\left(\Im\left(\overline{u_iu_j},\overline{u_i\theta},\frac{k}{\varepsilon},c_\theta\right)\right)}{\partial x_j}}_{\text{(b)}}\underbrace{-\overline{u_iu_j}\frac{\partial \overline{\mathrm{T}}}{\partial x_j}}_{\text{(e)}}\underbrace{-\overline{u_j\theta}\frac{\partial \overline{U_i}}{\partial x_j}}_{\text{(f)}}$$

$$\underbrace{\underbrace{+\Im\left(\overline{u_iu_j},\overline{u_i\theta},\frac{k}{\varepsilon},c_{\theta\,non-linear}\right)}_{non-linear}+\underbrace{\Im\left(\overline{U_i},\overline{u_i\theta},c_{\theta\,linear}\right)}_{linear}+\underbrace{\Im\left(\overline{U_i},\overline{u_i\theta},\frac{k}{\varepsilon},c_{\theta\,near-wall}\right)}_{near-wall}}_{\text{(g)}}$$

(1.18)

Turbulent flux models are a more rigorous way of solving for the turbulent heat flux because they involve fewer assumptions about the physical behaviour of turbulent eddies than gradient transport models. Consequently, these models can be applied to a wider range of velocity and scalar fields. However, the main disadvantage of turbulent flux models is the assumption that only one time-scale (the velocity field's time scale) k/ε, is used to describe the scalar field. Ideally, the integral time-scale of the scalar field, $k_\theta/\varepsilon_\theta$, should also be included in these models for instance in the form of a combined time scale, such as $\sqrt{(kk_\theta)/(\varepsilon\varepsilon_\theta)}$. ($k_\theta$ and ε_θ will be formally defined in the next section.) Unfortunately, the main reason for not introducing this time-scale is because two more unknowns will be added. Hence $k_\theta/\varepsilon_\theta$ is assumed to be "closely proportional" to k/ε, especially in cases where

"the same agency is responsible for generating both the velocity and the temperature fluctuations" (Launder, 1975).

1.2.2 Solving for the Passive Scalar Variance

In the previous section, the objective was to solve the Reynolds-averaged advection-diffusion equation for a passive scalar and thus obtain the mean scalar field. However, knowing only the mean scalar field can be insufficient in turbulence studies or engineering designs. Since there is no information about the fluctuating part of the flow, it is impossible to predict the range of values about the mean. Hence, to quantify the order of the scalar fluctuations, the root-mean-square of the passive scalar fluctuations, θ_{RMS}, needs to be determined. This is achieved by solving for the passive scalar variance, $\overline{\theta^2}$ $(=\theta_{RMS}^2)$, or alternatively $k_\theta (\equiv \overline{\theta^2}/2)$. The passive scalar variance budget is derived by multiplying $\left(AD - \overline{AD}\right)$ by θ, averaging , and multiplying all terms by 1/2. The result is:

$$\underbrace{\frac{\partial}{\partial t}\left(\frac{1}{2}\overline{\theta^2}\right)+\overline{U_j}\frac{\partial}{\partial x_j}\left(\frac{1}{2}\overline{\theta^2}\right)}_{\text{(a)}}=\underbrace{\alpha\frac{\partial^2}{\partial x_j \partial x_j}\left(\frac{1}{2}\overline{\theta^2}\right)}_{\text{(b)}}\underbrace{-\frac{\partial}{\partial x_j}\left(\frac{1}{2}\overline{\theta^2 u_j}\right)}_{\text{(c)}}\underbrace{-\overline{u_j\theta}\frac{\partial \overline{\mathrm{T}}}{\partial x_j}}_{\text{(d)}}\underbrace{-\alpha\overline{\frac{\partial\theta}{\partial x_j}\frac{\partial\theta}{\partial x_j}}}_{\text{(e)}}. \tag{1.19}$$

The table below interprets each term of the passive scalar variance budget:

	Term	Interpretation of the terms
Material derivative	(a)	time derivative and spatial convective derivative
Gradient terms	(b)	molecular diffusion
	(c)	transport due to the turbulent velocity fluctuations
Source and sink terms	(d)	production due to mean temperature gradients
	(e)	dissipation rate of scalar variance (ε_θ)

Table 1.2: Interpretation of the terms of the passive scalar variance budget

The goal is to model terms (b), (c), and (e) as a function of the "known" quantities, $\overline{\theta^2}$, $\overline{U_j}$, $\overline{T}$, $\overline{u_j\theta}$, and others, which already appear in terms (a) and (d). Once again, Schiestel (2008) provides a concise explanation of how each term is modeled by various turbulence modellers. Thus the remainder of this section will highlight the key points from this book.

An order of magnitude analysis shows that term (b) is negligible at high Reynolds and Péclet numbers. Modeling term (c) is similar to modeling the triple correlation term, $\overline{u_i u_j \theta}$ in the previous section. Hence, $\overline{\theta^2 u_j}$ is modeled by looking at its transport equation (which is derived in a similar manner to the transport equation of $\overline{u_i\theta}$ shown in sub-section 1.2.1.2):

$$\frac{D\overline{u_i\theta^2}}{Dt} = -\overline{u_j\theta^2}\frac{\partial \overline{U_i}}{\partial x_j} - 2\overline{u_i u_j}\theta\frac{\partial \overline{T}}{\partial x_j} - \frac{\partial \overline{u_i u_j \theta^2}}{\partial x_j} - \frac{1}{\rho}\theta^2\overline{\frac{\partial p}{\partial x_i}} + \overline{\theta^2}\frac{\partial \overline{u_i u_j}}{\partial x_j} + 2\overline{u_i\theta}\frac{\partial \overline{u_j\theta}}{\partial x_j}. \tag{1.20}$$

Having derived the transport equations for $\overline{\theta^2 u_j}$, additional unknowns are introduced; these also have to be modeled. Once all terms are modeled, $\overline{\theta^2 u_j}$ is expressed as a function of the following terms:

$$\overline{u_i\theta^2} = \Im\left(\overline{T}, \overline{u_i u_j}, \overline{u_i\theta}, \overline{u_i u_j \theta}, \frac{k}{\varepsilon}, c_q\right). \tag{1.21}$$

As discussed in section 1.2.1.2, only the velocity integral time-scale (k/ε) is used in this model instead of both the integral time-scale for the velocity field and the integral time-scale of the scalar field ($k_\theta/\varepsilon_\theta$).

To model term (e), ε_θ, the mechanical-to-thermal time-scale ratio, r, is introduced. r is defined as the integral time-scale of the turbulent velocity field divided by the integral time-scale of the turbulent scalar field (i.e. r is the proportionality constant between these two time-scales, assuming they are proportional):

$$r \equiv \frac{k/\varepsilon}{k_\theta/\varepsilon_\theta}. \tag{1.22}$$

Therefore, if r is specified, the dissipation term is found as follows:

$$\varepsilon_\theta = \frac{k_\theta}{r(k/\varepsilon)}. \tag{1.23}$$

r is usually assumed to be constant throughout the flow and is determined through experimental measurements.

A more general approach is to solve for ε_θ by deriving its transport equation and modeling each term. Using this approach, no assumption about the proportionality is necessary for relating $k_\theta/\varepsilon_\theta$ to k/ε. Various researchers have proposed modeled transport equations for ε_θ, but none agree. More experiments with simple turbulent flows are necessary to specify the numerical constants as no agreement has yet been reached (Schiestel, 2008).

1.2.3 Discussion

From the three types of approaches (DNS, LES, and RANS) used to predict the passive scalar field in turbulent flows, RANS-based models were the focus of section 1.2 since they are the least computationally intensive, provide practical quantities for engineering applications, and are widely used in industry. Typically, the

two main quantities of interest in engineering applications are: (i) the mean scalar field, and (ii) the scalar variance (to quantify the magnitude of the fluctuations).

To predict the mean scalar field, the turbulent heat flux term must be determined to close the Reynolds-averaged advection-diffusion equation. To model the turbulent heat flux term, the two common methods are: (i) to use the gradient transport hypothesis to model the turbulent heat flux, or (ii) to model each unknown term of the turbulent heat flux budget. The most widely used method in practical applications is the former due to its simplicity and lower computational cost. With this method, the turbulent heat flux is expressed in terms of the turbulent thermal diffusivity, α_T, and the mean scalar gradient. Thus, the unknown becomes α_T, which can quickly be determined by expressing it as ν_T / Pr_T. This expression can quickly evaluate α_T because ν_T is already obtained from the solution to the velocity field and Pr_T is an experimentally-determined constant.

The latter method deals with modeling the unknown terms of the turbulent heat flux budget. After making certain assumptions and performing an order of magnitude analysis, terms are neglected, and the turbulent transport of $\overline{u_i \theta}$ due to velocity fluctuations (referred to as term (b) in sub-section 1.2.1.2) and the redistribution term (referred to as term (g) in sub-section 1.2.1.2) are left to model. The models for these terms contain numerical constants, some of which are expressed as functions of Pr_T and other measurable quantities. Once again, Pr_T appears when attempting to predict the mean scalar field.

To predict the scalar variance, each unknown term of its transport equation is modeled. After simplifying the scalar variance budget by making appropriate

assumptions and performing an order of magnitude analysis, the turbulent transport of k_θ due to the velocity fluctuations (referred to as term (c) in sub-section 1.2.2) and the dissipation term (ε_θ) are left to model. ε_θ is modelled by two common methods: (i) introducing the mechanical-to-thermal time-scale ratio, r, and using the expression $\varepsilon_\theta = k_\theta / (r(k/\varepsilon))$, or (ii) modeling each unknown term of the transport equation of ε_θ. The former method is widely used because it is simpler and requires almost no additional calculations. However, it requires values of r which are estimated from experimental data. The latter method, although more rigorous, does not have a generally accepted model due to a lack of experimental data.

As highlighted in this section, Pr_T and r are two experimentally determined parameters that are important for modeling the passive scalar field in turbulent flows. The relative importance of these quantities is worth investigating to learn how they are measured, and what values are used for models. Therefore, a literature review of the work done in studying these parameters will be presented in the next section.

1.3 Literature Review

Turbulent flows, being a common occurrence in engineering applications, make the study of turbulence an important branch of fluid dynamics. There are several books and research papers written on turbulence. Two classic examples of books pertaining to the study of turbulence are “A First Course in Turbulence” by Tennekes and Lumley (1972) and “Turbulent Flows” by Pope (2000).

An interesting aspect of turbulence is the study of passive scalar mixing. As mentioned earlier, it is common to numerous scientific and engineering phenomena.

The mixing of a passive scalar in turbulent flows has received great interest for the last forty years. Warhaft (2000) presents a review on the work done over these years. Other reviews on this subject are done by Sreenivasan (1991), Shraiman and Siggia (2000), and Dimotakis (2005).

Experimentally, many simple turbulent flows with passive scalars have been studied. Theoretically, the simplest flows are homogenous, isotropic (usually grid-generated) turbulence because there is no mean velocity gradient (i.e., no shear). For this situation, the scalar is injected either by heating the grid or by heating an array of fine wires (called a mandoline) placed downstream of the grid. The second simplest types of flows are homogenous turbulent shear flows. Next there are inhomogeneous shear flows for which two main categories exist: (i) bounded shear flows which include boundary layers, channel flow, and pipe flow, and (ii) free shear flows which include mixing layers, jets, and wakes.

In the following sub-sections (1.3.1 and 1.3.2), the experimental results for Pr_T and r found in the literature for these simple turbulent flows will be summarized, respectively. Furthermore, basing their models on these experimental results, the values of Pr_T and r used by modellers will also be discussed.

1.3.1 The Turbulent Prandtl Number

The turbulent Prandtl number has been determined experimentally for a variety of simple turbulent flows. For bounded shear flows, Kays (1994) provides a review of about 50 papers ranging from the 1950s to the early 1990s on analytical, experimental, and DNS work done on Pr_T for two-dimensional turbulent boundary layers, and fully- developed flow in a circular tube or a rectangular duct. Pr_T results

are grouped into three flow regions: (i) the sublayer region, (ii) the "logarithmic" region, and (iii) the "wake" region of an external turbulent boundary layer, and the centerline region for fully-developed turbulent flow in a pipe. Furthermore, Pr_T for different types of fluids are considered; from fluids with low Pr (e.g., liquid metals) to fluids with very high Pr (e.g., transformer oil). Finally, the effect of pressure gradient, transpiration (blowing or suction), and surface roughness on Pr_T are separately examined for air.

Kays (1994) concludes that for the "logarithmic" region, Pr_T appears to be a function of the turbulent Péclet number, $\mathrm{Pe}_T (\equiv \nu_T / \alpha)$, and tends to 0.85 as Pe_T gets large (e.g., for gases and oils). When Pe_T is very small (e.g., for liquid metals), Pr_T grows indefinitely. After summarizing the results in the "logarithmic" region, Kays points out that in the sublayer region, Pr_T, for both air and water, is generally higher. As for the "wake" region and the centerline region for fully-developed turbulent flow in a pipe, Pr_T is between 0.5 and 0.7. Kays then discusses the pressure gradient effect on Pr_T for air. Experimental data suggest that Pr_T decreases with a positive pressure gradient and increases with a negative pressure gradient; however, other reports did not observe this trend. Thus, the effect of pressure gradient is said to be inconclusive. Finally, transpiration and surface roughness are shown to have little effect on Pr_T.

For free shear flows, table 1.3 summarizes the experimental results found by various authors. This table contains several symbols which are defined as follows: D represents the nozzle width for the plane jet and mixing layer at the plane jet exit, the diameter of the nozzle for the round jet, and the diameter of the cylinder for its wake. In addition, Re_D is the Reynolds number based on this parameter D. As for the

coordinates, x is the downstream distance from either the exit of the nozzle or the center of the cylinder; and y is the transverse coordinate in these two-dimensional flows. For the first table entry, h is used to non-dimensionalize the lateral coordinate and is defined as the velocity half-width (i.e., the value of y where the local mean velocity is half the mean centerline velocity).

There are two principal conclusions that can be drawn from this table: (i) the spatial distribution of Pr_T is not constant throughout a given flow, and (ii) the distribution of Pr_T appears to vary from one flow to the other (although the flow parameters in each flow are different, i.e., the measurements are made at different downstream positions and Reynolds numbers). Unfortunately, since both flow type and parameters are changed simultaneously, it is difficult to assess how each flow type or parameter affects Pr_T. Regardless, experimental evidence demonstrates that there is no universal constant value for Pr_T.

In contrast, when it comes to the use of Pr_T in engineering calculations, a constant value of Pr_T is often used throughout the flow in modeling of turbulent passive scalars for the sake of simplicity. Originally, the "Reynolds analogy" was used to justify the assumption that Pr_T is equal to unity (Tennekes and Lumley, 1972). Further investigation (i.e., compiling data from experiments and DNS) has lead to using other constant values of Pr_T based on the type of turbulent flow. Common values used are: $\mathrm{Pr}_T \approx 0.9$ for bounded-flows (Wilcox, 1993; Schiestel, 2008) and $\mathrm{Pr}_T \approx 0.5$ (Wilcox, 1993) or ≈ 0.7 (Pope, 2000; Schiestel, 2008) for free shear flows. In addition to simplicity, modellers justify using an averaged value of Pr_T because of the scatter in experimental results.

Authors	Turbulent Flow	Scalar Injection	Notes	Pr_T Distribution
Browne and Antonia (1983)	Plane jet	Jet heated by 1 kW electrical coil elements	$x/D = 20, 40$ $Re_D = 9\,939$	• 0.7 for $0 \le y/h \le 0.8$ • increasing monotonically from 0.7 to 1.2 for $0.8 \le y/h \le 1.5$
Chua and Antonia (1990)	Round jet	Jet heated by 1 kW electrical coil elements	$x/D = 15$ $Re_D = 17\,700$	• 0.81 ± 0.05 ($0 < y <$ the jet half-radius) • increasing in the outer region
Chang and Cowen (2002)	Round jet	Fluorescent dye injected	$Re_D = 360$	• $0.2 < Pr_T < 0.4$ for $0 < y/x < 0.15$ • 0.4 for $0.06 < y/x < 0.14$ • 0.2 near center and outer region
			$Re_D = 4\,210$	• $0.7 < Pr_T < 0.9$ for $0 < y/x < 0.12$ • decreasing monotonically for $y/x > 0.12$ • recommended value of $Pr_T = 0.8$ for high Reynolds number flows
Chambers, Antonia, and Fulachier (1985)	Mixing layer at the edge of the plane jet	Jet heated by 1 kW electrical coil elements	$x/D = 4, 5$ $Re_D = 7600$	• not constant distribution (0 to 0.8) • 0.4 in the region where the Reynolds stresses and heat fluxes are large
Antonia and Browne (1987)	Wake of cylinder	Cylinder heated electrically	$x/D = 270, 420, 600$ $Re_D = 1\,190$	• not constant distribution • covers the range of 0 to 1.2
Antonia, Zhou, and Matsumura (1993)	Wake of cylinder	Cylinder heated electrically	$x/D = 10, 20, 40$ $Re_D = 5\,830$	• not constant distribution • varies from 0.8 to 1.2 at $x/D = 10$ • varies from 0 to 1 at $x/D = 20, 40$

Table 1.3: Values of the turbulent Prandtl number found in literature

1.3.2 The Mechanical-to-Thermal Time-Scale Ratio

Like the turbulent Prandtl number, the mechanical-to-thermal time-scale ratio, r, has also been studied experimentally for a variety of simple turbulent flows. For grid-generated turbulence (i.e, homogeneous, isotropic turbulence), the variation in *r* was investigated by Warhaft and Lumley (1978), Sreenivasan, Tavoularis, Henry, and Corrsin (1980) and Durbin (1982). In grid-generated turbulence, the decay (downstream evolution) of the velocity and temperature fluctuations follows a power law: $\overline{u^2}/\overline{U}^2 = a(x/M)^{-n}$ and $\overline{\theta^2}/\overline{T}^2 = b(x/M)^{-m}$, where M is the grid mesh length, and a, b, n, and m are constants. For this flow, it can be shown that $r = m/n$. Warhaft and Lumley (1978) present the results from previous heated grid experiments and explain how the decay rate for the velocity fluctuations varied between $1.15 \le n \le 1.4$, but the decay rate for the temperature fluctuations varied over a much wider range $0.87 \le m \le 3.09$, which was dictated by the electrical power used to heat the grid. The conclusion from the heated grid experiments was that when injecting the scalar by heating the grid, changes in the heat supplied to the grid modified the scalar field. To avoid the dependence of the decay rate on the heat applied to the grid, a new scalar injection technique which did not affect the velocity field was developed; a "mandoline" (placed downstream of the unheated grid) is an array of fine, parallel wires. Using a mandoline, the temperature fluctuations had a decay rate which was independent of the applied heating. Furthermore, the mandoline allowed the length scale of the scalar field to be altered independently from that of the velocity field. Using different mandoline configurations (by varying its

downstream position and spacing between the wires), they found that the decay exponent m ranged from 1.29 to 3.20, thus concluding that r is not a constant.

Sreenivasan *et al*. (1980) performed similar experiments to Warhaft and Lumley in grid-generated turbulence where they used a heated screen (which does not alter the velocity field) placed downstream of the unheated grid. For the configurations they considered, they found that m was independent of the wire spacing, downstream position, and initial intensity of the fluctuations. The difference in the conclusions of these two papers was explained by Durbin (1982) who used a theoretical approach (Lagrangian dispersion theory). He explained that m depends on the ratio of the initial velocity-to-temperature length scales up to a value of 2.5, after which m is constant. Durbin pointed out that in Warhaft and Lumley's experiments the ratio of these length scales was in the 0.8 to 2.0 range and for Sreenivasan *et al.* the ratio was higher than 2.5.

More recently, Beaulac and Mydlarski (2004) studied the downstream evolution of m and r in inhomogeneous turbulence using the wake of a circular cylinder. Once again the mandoline was chosen as the scalar injection technique. The downstream location of the mandoline, the mandoline width, and the mandoline wire spacing were each varied to study the dependence on the initial conditions of scalar mixing. The following observations were made: (i) changing the downstream location of the mandoline (i.e., varying the velocity integral scale at the scalar injection point) with x/D = 2, 4, 10, and 20, resulted in m = 0.25, 0.40, 0.55, and 0.98, respectively. Results showed that all these different mandoline configurations did not influence the downstream evolution of r, for this reason r was spatially averaged (r_{av}). For the

above values of *x/D*, r_{av} = 1.21, 1.27, 1.39, and 1.80, respectively. (ii) Keeping the mandoline at one downstream position, *x/D* = 20, and using five configurations where the wire spacing, M_θ, and mandoline width, *W*, are varied (i.e., varying the scalar injection scale), gave the results shown in table 1.4.

W/D	M_θ/D	*m*	r_{av}
1	0.1	0.98	1.80
2	0.4	0.76	1.69
1	0.2	0.95	1.75
2	0.2	0.77	1.83
3	0.2	0.58	1.68

Table 1.4: *m* and *r* results to different scalar injection scales (adapted from Beaulac and Mydlarski, 2004)

The authors concluded that changes in the velocity integral scale at the scalar injection point affects the scalar field in a similar way as observed in grid-generated experiments, i.e., as *m* increased, r_{av} increased. However, changes in the scalar injection scale caused almost no variations in r_{av}, but caused variations in *m*. Consequently, the downstream evolution of the scalar field (*m*) can be modified without changing the structure of the flow (r_{av}). These results are different from those in grid-generated turbulence where *r* is directly linked to *m* with *r* = *m*/*n* (which is proven by simplifying the turbulent kinetic energy and scalar variance budgets). The authors therefore theorized that the independence of *m* and *r* is a result of the inhomogeneous nature of the flow.

Using experimental data available in the literature, Béguier, Dekeyser, and Launder (1978) evaluated the distribution of *r* for various thin shear flows: (i) the turbulent boundary layer over a heated flat plate (from three papers), (ii) fully-developed pipe flow (from two papers), (iii) near the centerline region of the wake of

a heated cylinder (from one paper), (iv) asymmetrically heated mixing layer (from one paper). The authors concluded that for these various thin shear flows, the distribution of r is around 2 (ranging from 1.5 to 2.5).

In summary, the effect of scalar injection on the downstream evolution of r was studied for homogeneous, isotropic turbulence and inhomogeneous turbulence. The distribution of r at a given downstream position was also studied for a variety of inhomogeneous turbulent flows. These results demonstrate that r is generally not a constant and varies from flow to flow. In contrast, modellers use constant values such as $r = 1$ for homogeneous, isotropic turbulence (Launder, 1976), or simply $r = 2$ for all flows (Pope, 2000).

1.4 Thesis Objective and Overview

1.4.1 Thesis Objective

The main objective of the present work is to experimentally study scalar mixing in turbulent flows with applications to the modeling of turbulent passive scalars. Having presented how the turbulent passive scalar field is modelled (section 1.2), the parameters Pr_T and r were of interest. Furthermore, doing a literature review on the experimental work done on these quantities showed that there is significant variation in measured values from one flow to the next. Part of this variation may be due to the flows or different parameters for the same flow (measurement location, Reynolds number, and so on) used in the experiments. It is of practical benefit to quantify the variations in Pr_T and r that can be expected between fundamental experiments and "real" complex flows. Therefore, to determine this

variation (without any extraneous differences due to variations in flow parameters), this work will investigate the sensitivity of Pr_T and r for one type of flow (with constant flow parameters) for two different passive scalar injection methods. This will be of use since it will provide us with estimates of the variability of Pr_T and r for a given type of flow because (i) no modelled flow is exactly the same as that for which experiments were performed, and (ii) we will be able to determine how much of the variability is from sources other than flow parameters.

The flow under consideration is the turbulent wake of a circular cylinder. The passive scalar (temperature) is injected in one of two ways: (i) by heating the cylinder, and (ii) by heating an array of fine wires (a mandoline) placed downstream of the cylinder. Hot-wire anemometry and cold-wire thermometry are used for measuring velocity and temperature, respectively, in this work.

1.4.2 Thesis Overview

This thesis is divided into five chapters. Chapter 2 describes the experimental set-up, calibration procedures, data acquisition and analysis. In Chapter 3, the velocity and scalar fields are presented and validated individually. The results are presented and discussed in Chapter 4. Finally, Chapter 5 presents conclusions and suggestions for future work.

Chapter 2: Experimental Setup

2.1 The Wind Tunnel

The experiments were performed in a low-background-turbulence, open-circuit, suction-design wind tunnel (shown in figure 2.1) located in the Aerodynamics Laboratory at McGill University. The flow conditioning section of the wind tunnel consists of an aluminum honeycomb, four screens of stainless steel wire mesh, and a 9-to-1 area ratio contraction that follows a fifth degree polynomial profile.

Figure 2.1: Wind tunnel in which the present experiments were undertaken

Following the contraction is the test section. It is 0.853 m high, 1.22 m wide, and 2.74 m long with bevelled corners that slowly decrease in length in the downstream direction (increasing the cross-sectional area) to maintain a constant free-stream velocity throughout the test section. The test section is followed by an 8.84 m-long small-angle diffuser, and an axial fan. The fan is powered by a 125 hp

AC motor, with a controller that is accurate to within ±1 rpm (ensuring the stability of the mean flow). The experiments were conducted at a nominal mean flow velocity of 7.34 m/s with the measurements made at 40 diameters downstream of the center of the cylinder.

2.2 The Cylinder

A cylinder of circular cross-section was used to generate a turbulent wake. It was placed vertically, along the tunnel's midplane, at the entrance of the test section. The cylinder is made of a 5.08 cm outer diameter aluminum pipe with 1.984 mm (5/64") wall thickness. Its length spans the entire height of the test section with end supports fixed to the walls of the wind tunnel (see figure 2.2).

Figure 2.2: The cylinder (seen on the right) placed in the test section of the wind tunnel

Two methods were used to heat the wake of the cylinder. The first method involved heating the cylinder itself. Inside the cylinder is (i) a 1.5 kW tubular electric heating element with an external diameter of 0.635 cm (¼"), and (ii) a series of concentric thermal fins (25 mm in length) that fill the gap between the outer surface of the element and the inner surface of the aluminum pipe. To guarantee a uniform, axisymmetric temperature distribution on the outside surface of the cylinder, high-thermal-conductivity paste was applied to the thermal fins. The element was heated using a variable AC power supply (1.5 kW) and was electrically insulated from the aluminum pipe.

2.3 The Mandoline

The second method used to create the thermal wake is a "mandoline". Developed by Warhaft and Lumley (1978), the mandoline is an array of fine, parallel, heated wires placed downstream of the unheated cylinder and parallel to the axis of the cylinder (see figure 2.3). The mandoline configuration used in this work consisted of thirteen 0.127 mm diameter nichrome (type A) wires, spaced 5.08 mm apart, resulting in a total width of 61.0 mm. The wires were heated using a variable DC power supply providing 1.1 kW of power. Small springs were attached at one end of each wire to maintain tension since the wires expand when heated. Furthermore, the mandoline's two end mounts were electrically and thermally insulated using small ceramic plates. The diameter of the wires, d_{wire}, was chosen such that the Reynolds number, $\mathrm{Re}_{d_{wire}} = \overline{U} d_{wire} / \nu < 40$ to prevent shedding of vortices (Lienhard and Lienhard, 2008). (ν is the kinematic viscosity of air evaluated at the film

temperature, $T_{film} = 0.5(T_{wire} + T_{\infty})$, with T_{wire} being the temperature of the mandoline's wire and T_{∞} being the free-stream temperature.)

Figure 2.3: The mandoline (top half seen on the left) placed in front of the cylinder

Figure 2.4 shows a schematic of the experimental setup in the test section. U_{∞} represents the (constant) free-stream velocity that flowed past the cylinder of diameter, *D*. The origin of the coordinate axes, *x* and *y*, was located at the center of the cylinder. The mandoline was placed at a downstream distance of *x/D* = 10 (noting that when the mandoline was used to heat the wake, the cylinder was not heated, and when the cylinder was used to heat the wake, the mandoline was removed from the wind tunnel). The sensors were placed at *x/D* = 40 and were mounted on a traversing mechanism which moved in the transverse (*y*) direction.

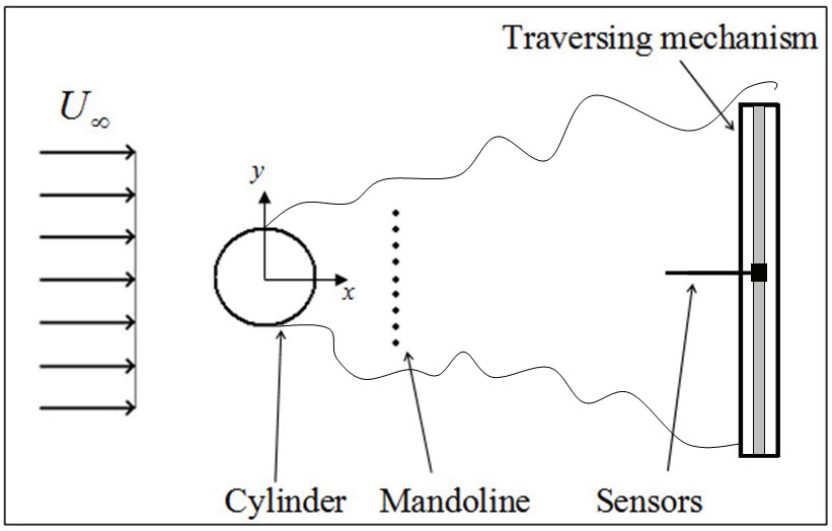

Figure 2.4: Schematic of the experimental setup (top view, not to scale). Note that *x* represents the downstream or longitudinal direction and *y* represents the transverse direction.

2.4 The Measurement Instruments

Cold-wire thermometry (CWT) and hot-wire anemometry (HWA) are discussed in "Hot-Wire Anemometry: Principles and Signal Analysis" by Bruun (1995). The advantages of using such techniques include: relatively low-cost, high-frequency response, compact, continuous signals provided, good signal-to-noise-ratios, and length scales on the order of the smallest (Kolmogorov) scale for many flows.

Cold-wire thermometry measurements were made using a constant current anemometer (CCA). A cold-wire sensor is a fine cylindrical wire with a low constant current passing through it. The resistance of the wire changes linearly with temperature (for small enough temperature changes); consequently the output voltage varies linearly with temperature. The CCA, used for the temperature measurements, was built at Université Laval. The sensor was a Wollaston wire with a 0.625 μm-diameter platinum core mounted on a TSI 1210 single-wire probe (shown in figure

2.5). The resistance of the cold-wire was around 150 Ω, corresponding to a length-to-diameter ratio on the order of 800. This ratio is lower than the recommended value given by Browne and Antonia (1987) who recommended a ratio of 1500 to guarantee reduced conduction between the wire and the prongs. However, for better spatial resolution, they also recommended that the length of the wire (l_w) be no greater than five times the Kolmogorov microscale (i.e., the smallest length scale in the velocity field), η. In this flow, $l_w / \eta \approx 4$; hence, a length-to-diameter ratio on the order of 800 was a good compromise between these two competing effects (Mydlarski and Warhaft, 1998).

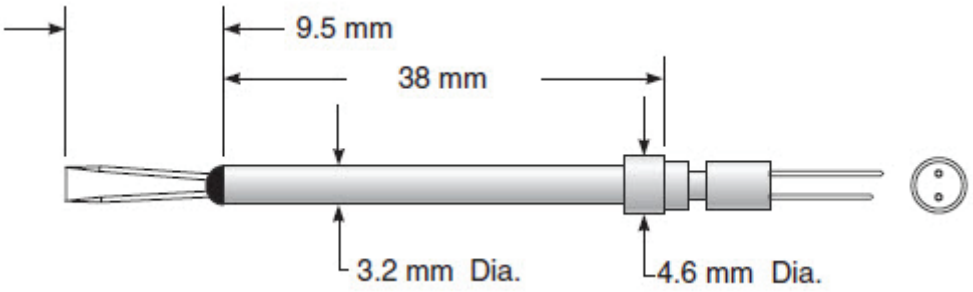

Figure 2.5: TSI 1210 single-wire probe (image from tsi.com)

For longitudinal and transverse velocity measurements, hot-wire anemometry (HWA) in the constant temperature anemometer (CTA) mode was used. A hot-wire sensor is a fine cylindrical wire electrically heated and maintained at a constant temperature (i.e., resistance), much higher than the flow's temperature, by the anemometer. As the wire is being convectively cooled by the fluid flow, the anemometer supplies additional voltage to maintain the wire at this temperature. This applied voltage is the recorded output of the anemometer. To this end, a two-channel TSI IFA 300 anemometer was employed. The sensors were made using 3 μm

diameter tungsten wires (with a copper coating) separated by a distance of 1 mm, and mounted on a TSI 1241 X-probe (shown in figure 2.6). The copper coating was etched away with nitric acid, thus revealing the sensing portion of the wire. The resistance of each sensor is around 5 Ω which corresponds to a length-to-diameter ratio of about 200.

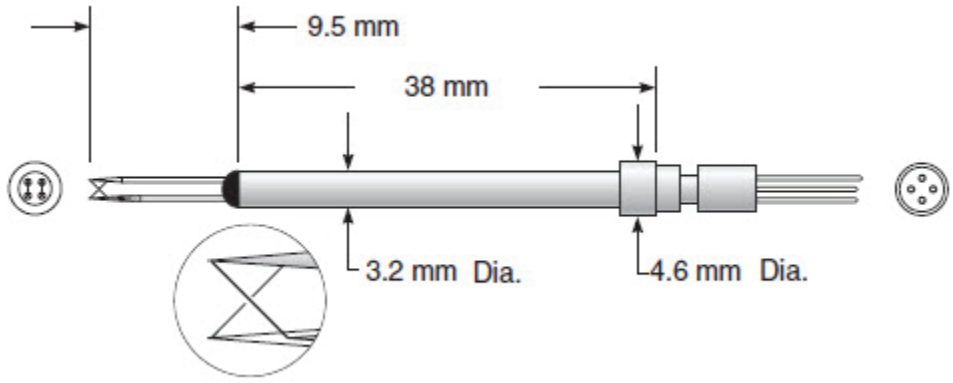

Figure 2.6: TSI 1241 X-probe (image from tsi.com)

To make simultaneous velocity-temperature measurements, the X-probe was mounted beside the cold-wire probe. The cold-wire was located 1 mm from the nearest hot-wire and 0.25 mm upstream from the centre of the X-probe to prevent contamination of the temperature measurements due to the hot wake of the X-probe (see figure 2.7). Beaulac (2003) measured the velocity field with and without the cold-wire probe beside the X-probe and found no significant difference in the velocity measurements.

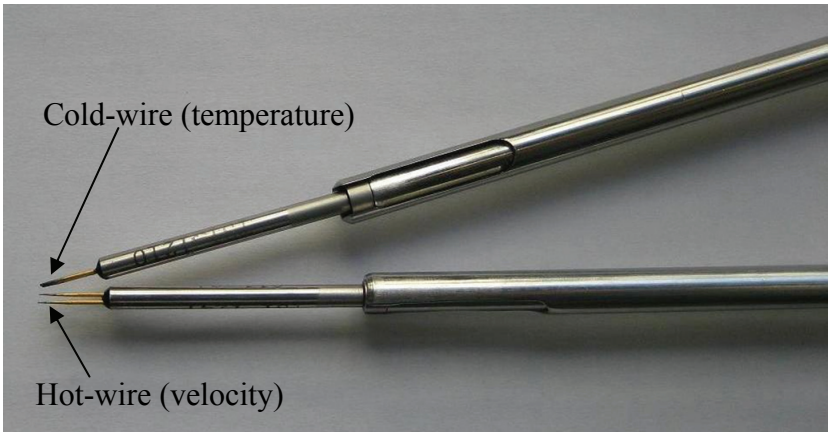

Figure 2.7: Velocity and temperature probe arrangement

2.5 Calibration Procedures

The recorded output for both the cold- and hot-wires is voltage; however, each type of wire relies on different physical principles to make the measurements. Therefore, each wire has a distinct calibration procedure, which is described in sub-section 2.5.1 for the cold-wire probe, and in sub-section 2.5.2 for the hot-wire probe.

2.5.1 Cold-Wire Calibration

Before calibrating a cold-wire sensor, the current of the constant-current anemometer is set. The current is selected based on the diameter of the wire; for a 0.625 μm diameter wire, the recommended current is 0.10 mA (Lemay, private communication). This choice is based on a balance between two competing effects: (i) if the current is too high, the wire becomes too hot and starts sensing velocity fluctuations and (ii) if the current is too low, the signal-to-noise ratio becomes unacceptably small. For small temperature differences, and using Ohm's law, it can be shown that the output voltage, E, varies linearly with temperature as follows:

$$T = C \times E + D, \tag{2.1}$$

where C and D are calibration constants determined by a least-squares fit to the calibration data.

To calibrate the cold-wire sensor, a heated, circular, laminar jet was used. The jet's velocity was set to a constant value similar to the experiment's mean velocity. The air jet was heated using three 120 W electric heaters which were attached to the outside of a 5.08 cm diameter copper pipe connected to the calibration jet's air supply. Once the air is heated to a temperature above that of the ambient temperature (about 15 to 20°C above), the electric heaters are turned off allowing the jet to cool down. After a certain time, the jet's temperature decreases monotonically, at which time calibration can begin. The output voltage of the CCA and the air temperature at the exit of the jet are simultaneously measured. A typical calibration curve is presented in figure 2.8.

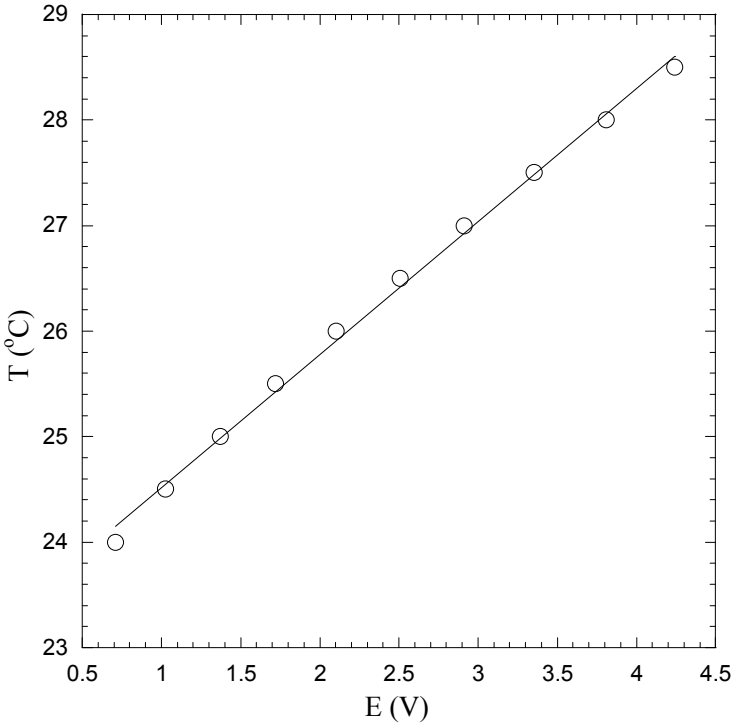

Figure 2.8: Typical temperature calibration curve

The time constant of the cold-wire, τ_w, was then measured to determine the wire's cut-off frequency, $f_c \equiv 1/(2\pi\tau_w)$. f_c is the natural frequency of the cold-wire, representing the response of the wire to a change in temperature (resistance). The purpose of finding f_c was to verify the temporal resolution of the cold-wire: if f_c is significantly smaller than the highest frequency in the flow (i.e., the Kolmogorov frequency), the temperature fluctuations will be unresolved in time.

τ_w was measured using the current injection technique proposed by Lemay and Benaïssa (2001). This technique requires passing a square-wave current through the cold-wire causing the wire's temperature to rise by about 20 °C above the ambient temperature during the high current periods. As the wire cools by forced convection, the time constant can be determined; the response of the wire to a square-wave current was recorded (i.e., the CCA output voltage vs. time was recorded). The following equation was proposed by Lemay and Benaïssa (2001) to model the output of the CCA in response to the current injection:

$$E = C_1 e^{-t/\tau_E} + C_2 e^{-t/\tau_w} + C_3 . \tag{2.2}$$

This equation represents the cooling period of the cold-wire described by an exponential decay due to the electronics superimposed with an exponential decay due to the wire's thermal time constant. Equation 2.2 was least-squares fit to the data (see figure 2.9) with τ_E being the time constant of the electronics (herein, τ_E=3μs). Hence, the constants C_1, C_2, C_3, and τ_w were determined and f_c was calculated from its definition, $f_c \equiv 1/(2\pi\tau_w)$.

For a given mean flow velocity and cold-wire diameter, f_c can be predicted theoretically. However, the actual value of f_c may be lower due to dust (and other types of contaminating debris) or some coating/fouling of the wire. Therefore, f_c was determined after each cold-wire calibration and before each experiment to check the state of the cold-wire. If f_c is too low, the cold-wire was cleaned with isopropanol (rubbing alcohol) to improve its frequency response.

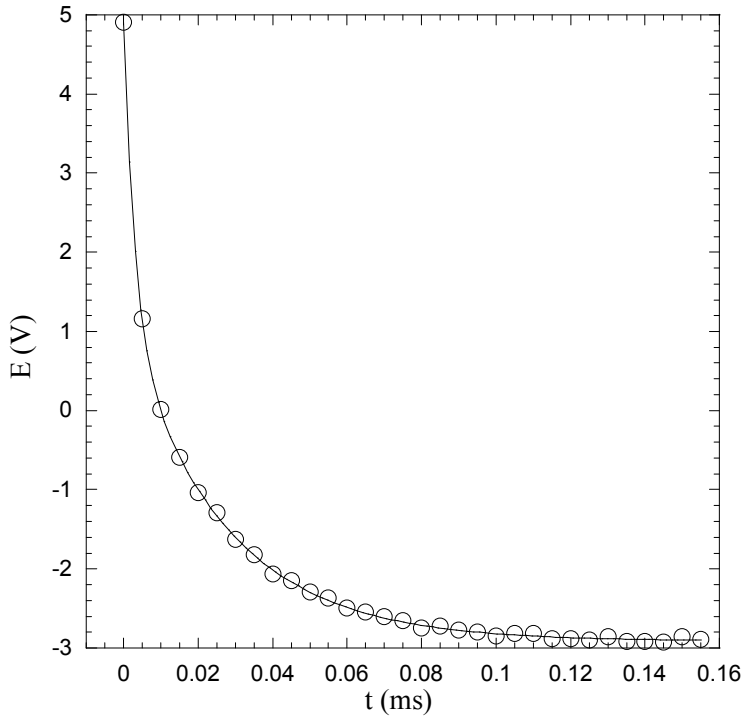

Figure 2.9: Cold-wire temporal response to the current injection technique

2.5.2 Hot-Wire Calibration

Hot-wires operate at a high (constant) temperature, as mentioned earlier. The operating temperature (or resistance) for each hot-wire is set by selecting an overheat ratio (i.e., the ratio of the resistance of the heated wire to the resistance of the wire at ambient temperature) of 1.8, which corresponds to a wire temperature of

approximately 240°C (Bruun 1995). Since hot-wires operate significantly above the ambient temperature, before performing any calibration, newly made hot-wires must be "aged" (or "burned in"). In other words, the wires are operated for at least 24 hours to allow the material properties to reach a steady-state. (Note that since cold-wires operate at ambient temperature, aging is not necessary.)

The calibration procedure for hot-wires is more complex than that of cold-wires because the anemometer response to flow velocities is non-linear. The relationship between velocity and voltage is predicted by a modified King's Law:

$$E^2 = A + B \cdot U^n, \tag{2.3}$$

which can be derived using a forced convection heat transfer analysis of a heated cylinder. A, B, and n are the calibration constants determined by a least-squares fit to the calibration data.

Relationship 2.3 is applicable to isothermal flows. However, in these experiments, the flow is non-isothermal. Therefore, to account for the temperature changes, Lienhard (1988) proposed the following corrections to constants A and B (in equation 2.3), based on heat transfer principles and on the empirical effect of temperature on fluid properties:

$$A = \overline{A}\left(\frac{T + T_{w,a}}{2}\right)^{0.84}\left(T_{w,a} - T\right), \tag{2.4}$$

$$B = \overline{B}\left(T_{w,b} - T\right), \tag{2.5}$$

where T is the varying flow temperature and $\overline{A}$, $\overline{B}$, $T_{w,a}$, and $T_{w,b}$ are constants determined by the calibration. $T_{w,a}$ and $T_{w,b}$ are representative of the operating temperature of the hot-wires.

To calibrate the hot-wires, the X-probe was placed in the round jet and was aligned in the direction of the mean flow (x-direction) resulting in each hot-wire being nominally inclined at about 45° to the flow. The jet velocity was varied while maintaining different (constant) jet temperatures by setting the electric heaters to a certain power and allowing the system to reach steady-state. The variation of the jet temperature for one King's Law calibration was at most ±1.2 °C. The velocity was varied from about 4 m/s to 19 m/s, covering the range of velocities encountered in the experiments. Therefore, five calibrations (recording the velocity and the anemometer output voltage) were performed at five different temperatures. Figure 2.10 shows an example of this calibration for one of the hot-wires.

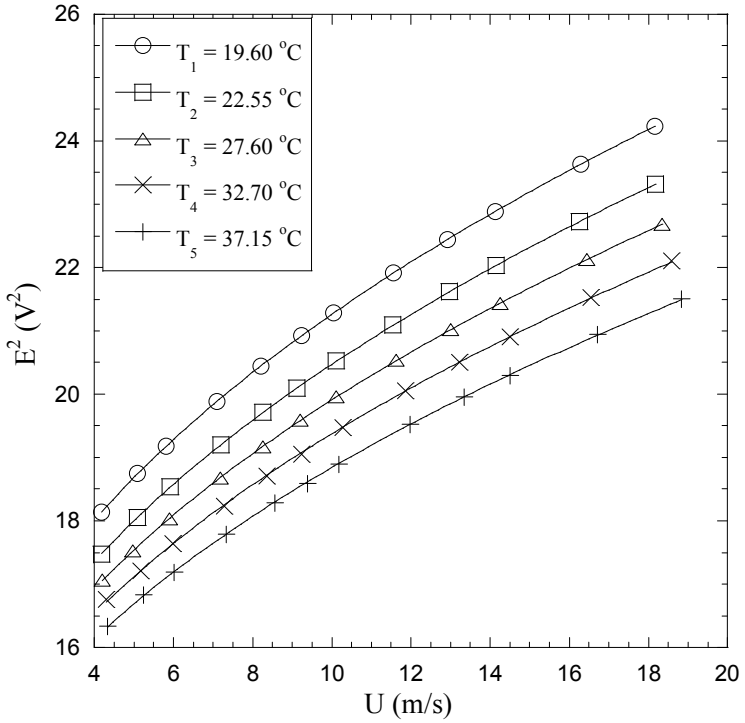

Figure 2.10: Typical calibration curves for a hot-wire of an X-probe, (n = 0.44975)

To determine the calibration constants $\overline{A}$, $\overline{B}$, $T_{w,a}$, and $T_{w,b}$, the following procedure was applied: (i) King's Law (equation 2.3) was fitted (in the least-squares

sense) to the E^2 vs. U data set for each temperature to find five different *n*'s. (ii) Taking the average value of the exponent *n* (which is approximately temperature independent), King's Law, using this average value of *n*, was fitted to the E^2 vs. U data set (as shown in figure 2.10) to find A and B for each free-stream temperature, T. Finally, (iii) equation 2.4 was fitted to the A vs. T data to determine $\overline{A}$ and $T_{w,a}$, and equation 2.5 was fitted to the B vs. T data to determine $\overline{B}$ and $T_{w,b}$.

The two hot-wires mounted on the X-wire probe were cooled by both cross- and parallel-flow since they are not perpendicular to the flow. With the output voltages from each wire (E_1 and E_2), the velocities, U_1 and U_2, corresponding to the output voltages from each wire, were determined from equation 2.3. To determine the longitudinal and transverse velocity components from U_1 and U_2, the effective angle method described by Browne *et al.* (1989) was followed.

The effective angle method considers a hot-wire recording a CTA output voltage, *E,* to measure an instantaneous velocity, U, at some inclination to this hot-wire. The effective velocity, U_{eff}, is introduced as the velocity, that, if it were normal to the wire, would produce the same voltage *E* as U. The relationship between U_{eff} and U is defined as:

$$U_{eff} \equiv U f(\theta_{eff}), \tag{2.6}$$

where $f(\theta) = (\cos^2\theta + k^2 \sin^2\theta)^{1/2}$ and k^2 is used to account for the effect of longitudinal cooling. Browne *et al.* (1989) set k^2 to a standard constant value (and independent of the orientation of the wire with respect to the flow) of 0.03. θ_{eff} is the effective angle and is approximately equal to the angle between the mean flow and

the "normal" of the hot-wire. (The value of θ_{eff} also depends on factors such as the curvature of the wire, non-conventional heat transfer from the wire, etc.).

θ_{eff} of each hot-wire is obtained by means of a yaw calibration. The X-probe is calibrated using 9 different yaw angles ranging from -24° to 24° in increments of 6° at ambient temperature (because θ_{eff} is independent of temperature) and at a fixed jet speed. θ_{eff} for each yaw angle is determined, then averaged to give the effective angle of each hot-wire.

Once θ_{eff} for each hot-wire is known, the longitudinal and transverse velocity components can be determined as follows: say the two inclined hot-wires experience the same instantaneous velocity, S, at an angle β, from the mean flow direction (shown in figure 2.11 with θ_1 and θ_2 as the effective angle of each hot-wire). U_1 and U_2 are the velocities corresponding to the output voltages from each wire, E_1 and E_2. Assuming that the effective velocity (i.e., the velocity normal to the hot-wire) due to S is the same as the effective velocity due to U_1 for one hot-wire and U_2 for the second hot-wire, the following equations are obtained:

$$U_1 f(\theta_1) = S f(\theta_1 - \beta), \tag{2.7}$$

$$U_2 f(\theta_2) = S f(\theta_2 + \beta). \tag{2.8}$$

The instantaneous longitudinal ($\widetilde{U}$) and transverse velocity ($\widetilde{V}$) components can be determined by solving for S and β from these two equations. Hence, $\widetilde{U} = S\cos\beta$ and $\widetilde{V} = S\sin\beta$.

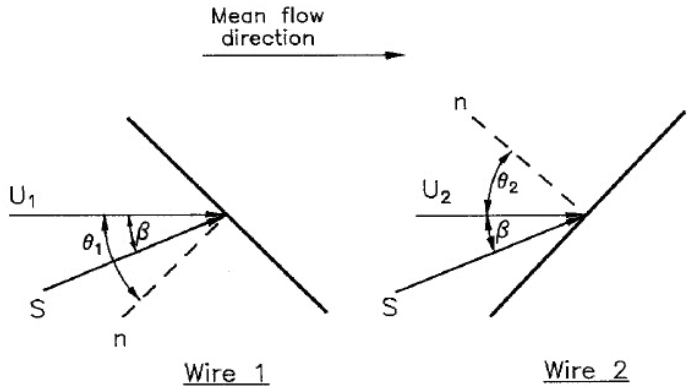

Figure 2.11: Top view of the X-probe wires, shown separated (figure from Browne *et al.*, 1989)

Table 2.1 shows the typical calibration constants for the two channels (two hot-wires) of the X-probe.

Anemometer channel	1	2
n	0.44677	0.44975
$\overline{A} \times 10^4$	3.0976	3.4232
$\overline{B} \times 10^2$	2.9243	3.1155
$T_{w,a}$	529.56	510.58
$T_{w,b}$	409.59	401.81
θ_{eff}	-44.108	-45.657

Table 2.1: Typical X-probe calibration constants

The frequency response of the hot-wires is faster (on the order of 100 kHz) than that of cold-wires due to the nature of the CTA system. The anemometer specifications state the frequency response to be 260 kHz for a 3.8 μm-diameter wire and a flow velocity of 100 m/s. Since the maximum frequency encountered in the present flow was on the order of 10 kHz, the temporal resolution of the hot-wires is a non-issue.

2.6 Data Acquisition and Analysis

For temperature measurements, the output signal from the CWT was connected to a Kron-Hite model 3384 where it was low- and high-pass filtered. The

mean output voltage was recorded separately to be able to determine the mean temperature (needed for A and B, two constants used to determine velocity). For velocity measurements, the output signal from the CTA was given a DC offset from the anemometer output voltage (that was approximately equal to the anemometer mean output voltage). This signal was then low-pass filtered using the same filter as the CWT.

After being filtered, an oscilloscope was used to monitor the signal from each channel and to determine the voltage span over which the data should be acquired (to make full use of the bits of the data acquisition (DAQ) board). The analogue signals were then converted to digital using a National Instrument PCI-6036 16-bit DAQ board. This DAQ board was controlled using LabVIEW 7.0.

The high-pass filter was set to 0.1 Hz for the cold-wire's channel and the low-pass filter was set to the maximum frequency of the flow at the centerline. The low-pass frequency for each wire was estimated with a real-time spectrum analyzer, which was created by a Virtual Instrument controlled by LabVIEW. These maximum frequencies were slightly larger than the Kolmogorov frequency for the two fields.

Velocity and temperature measurements were assumed to be taken simultaneously even though the DAQ has an inter-channel delay of 5 μs. This assumption is valid because the time lag is only 0.04 % of the Kolmogorov (smallest) time scale.

Two types of data sets were acquired: (i) for large-scale statistics, and (ii) for spectra. For large-scale statistics the values must be statistically independent from one another; hence a sampling frequency on the order of the integral time scale was necessary. The sampling frequency was set to 200 Hz with 10 blocks of 4096 samples

each (for a total of 40 960 data points). For "spectral" data, the sampling frequency was set to twice the low-pass frequency (in accordance with the Nyquist criterion) with 400 to 3000 blocks of 16 384 samples.

The data was then processed using a computer code (written in FORTRAN 90) that converts the acquired data (voltages) to physical quantities (i.e., velocity or temperature) using the calibration constants and then performs various statistical analyses of the results.

To improve the small-scale measurements for the cold-wire thermometer, a compensation method was employed. The compensation procedure was applied when the cut-off frequency of the cold-wire, f_c, (see section 2.5.1) was lower than two times the Kolmogorov frequency (as recommended by Lemay and Benaïssa, 2001). The compensation procedure consists of multiplying the Fourier transform of the original signal by the filter function, $H_f(f)$, put forth in Lemay and Benaïssa (2001), and defined as follows:

$$H_f(f) = \left|H_f(f)\right| e^{-j\phi(f)}, \tag{2.9}$$

with

$$\left|H_f(f)\right| = \sqrt{\frac{1+(f/f_c)^2}{1+(f/f_c^{'})^2}}, \tag{2.10}$$

as the filter gain, where $f_c^{'}$ is the low-pass frequency, and

$$\phi(f) = -\tan^{-1}\left(\frac{f}{f_c}\right), \tag{2.11}$$

as the phase. The compensated signal was then obtained by taking the inverse Fourier transform of this product:

$$\theta(t)_{\text{compensated}} = F^{-1}\left\{H_f(f)\Theta(f)_{\text{uncompensated}}\right\}. \tag{2.12}$$

Figure 2.12 shows the compensated and uncompensated dissipation spectra at the centerline. As explained earlier, the small scales which are represented by the large frequencies are the ones that need the correction.

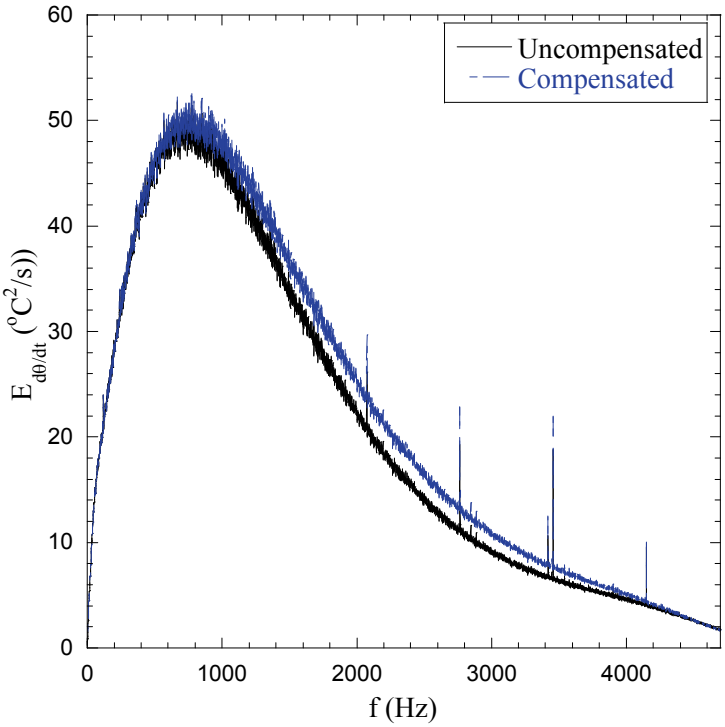

Figure 2.12: Uncompensated and compensated cold-wire signal

Chapter 3: Flow Characteristics

In this chapter, the characteristics of the (individual) velocity and temperature field will be presented. The overall properties of the flow (i.e., its symmetry and two-dimensionality) will be discussed. Furthermore, the influence of the mandoline on the flow and the passivity of the scalar will be verified.

3.1 The Velocity Field

When a uniform stream in the *x*-direction flows over a circular cylinder having its axis aligned with the *z* axis, a turbulent wake is formed. In this instance, the structure of the flow changes in the downstream direction — the velocity field is said to be *evolving* in the direction of the mean flow. Three main regions characterize the evolution of the hydrodynamic wake: (i) the near wake ($x/D \leq 5$), (ii) the intermediate wake, $5 \leq x/D \leq 50$, and (iii) the self-preserving far wake, $x/D >$ hundreds of diameters (Matsumura and Antonia, 1993). Precise values of the limits between these regions are difficult to obtain because they depend on parameters such as the Reynolds number.

In this work, measurements were made in the intermediate region at a downstream position of *x/D* = 40 with a free stream velocity of $U_\infty = 7.34$ m/s corresponding to a Reynolds number (based on the cylinder's diameter $\mathrm{Re}_D = U_\infty D/\nu$) of $\mathrm{Re}_D = 24\ 260$.

3.1.1 Parameters of the Velocity Field

To describe the velocity field generated herein, six flow parameters are studied (for both the longitudinal and transverse velocity components). (i) The root mean square (RMS) of velocity, defined as $u_{RMS} \equiv (\overline{u^2})^{1/2}$, quantifies the order of magnitude of the velocity fluctuations. (ii) The skewness, $S_u \equiv \overline{u^3}/(\overline{u^2})^{3/2}$, quantifies the (positive/negative) symmetry of the statistical distribution of the velocity fluctuations. (iii) The kurtosis (or flatness), $K_u \equiv \overline{u^4}/(\overline{u^2})^{4/2}$, quantifies the likelyhood of very large velocity fluctuations. (iv) The dissipation rate of turbulent kinetic energy, $\varepsilon \equiv 2\nu\,\overline{s_{ij}s_{ij}}$ (described in sub-section 1.2.1.2), which quantifies the rate at which the turbulent kinetic energy is converted to internal energy, is determined by assuming small-scale isotropy and using Taylor's frozen flow hypothesis:

$$\varepsilon = 15\nu\left[\overline{\left(\frac{du}{dx}\right)^2}\right] = \frac{15\nu}{\overline{U}^2}\left[\overline{\left(\frac{du}{dt}\right)^2}\right]. \tag{3.1}$$

Taylor's frozen flow hypothesis implies that changes in the downstream direction can be related to time as $t = -x/\overline{U}$ and can be used when the turbulence intensity, $u_{RMS}/\overline{U}$, is much smaller than unity. In the present work's experiments, $u_{RMS}/\overline{U}$ is on the order of 10%; hence the use of Taylor's frozen flow hypothesis throughout the flow is applicable. (v) The integral length scale, ℓ, quantifies the largest length scale of the flow and is determined by evaluating the integral of the auto-correlation function up to its first zero, as suggested by Comte-Bellot and Corrsin (1971). (vi) The Kolmogorov scale, η, quantifies the smallest length scale of the flow and is defined as:

$$\eta \equiv (\nu^3 / \varepsilon)^{1/4} . \tag{3.2}$$

The flow parameters at the centerline are summarised in table 3.1. These velocity measurements are made without the presence of the mandoline placed in the flow.

x/D	40
$\overline{U}$ (m/s)	6.33
u_{RMS} (m/s)	0.590
v_{RMS} (m/s)	0.523
S_u	0.099
S_v	-0.006
K_u	2.81
K_v	2.79
ε (m^2/s^3)	2.48
ℓ (mm)	110
η (mm)	0.20

Table 3.1: Flow parameters at the centerline

In addition to the six flow parameters discussed, it is beneficial to consider the distribution of the turbulent kinetic energy from the largest eddies (integral scale), to the smallest eddies (Kolmogorov scale), by means of the power spectrum (or power spectral density) of the velocity fluctuations. Figure 3.1 plots the power spectrum of u and v at the centerline. As expected, these plots indicate that the majority of the contributions to the turbulent kinetic energy come from the smallest frequencies, which correspond to the largest eddies. Also, for both figures, a sharp peak in the v spectrum occurs at a frequency of about 30 Hz. This frequency corresponds to the vortex shedding frequency, f_v, calculated from the Strouhal number, $S_t = f_v D / U_\infty = 0.21$ (Kovásznay, 1949).

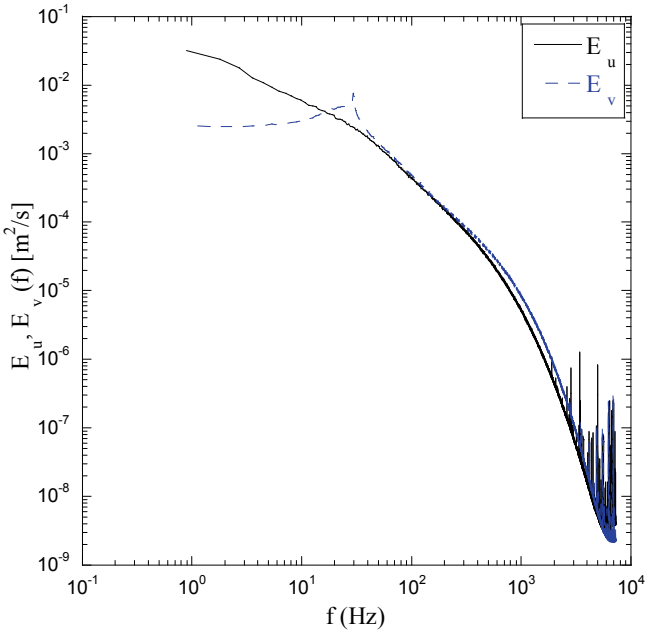

Figure 3.1: Power spectrum of *u* and *v* at the centerline

3.1.2 Structure of the Hydrodynamic Wake

3.1.2.1 Symmetry of the Hydrodynamic Wake

The mean longitudinal velocity profile is shown in figure 3.2. (Note that angular brackets, e.g., <*U*>, are sometimes used to identify the mean of a quantity.) The profile is symmetric about the $y = 0$ axis. This profile is predicted theoretically (Tennekes and Lumley, 1972) to be Gaussian, assuming self-similarity and a constant turbulent viscosity throughout the wake. Hence the following equation can be used to describe the mean velocity:

$$\overline{U} = A - Be^{\frac{-(y/D - y_o/D)^2}{2\sigma^2}}, \tag{3.3}$$

where $A = U_\infty$, B is a constant, σ is the standard deviation, and y_o / D is any small offset that might exist.

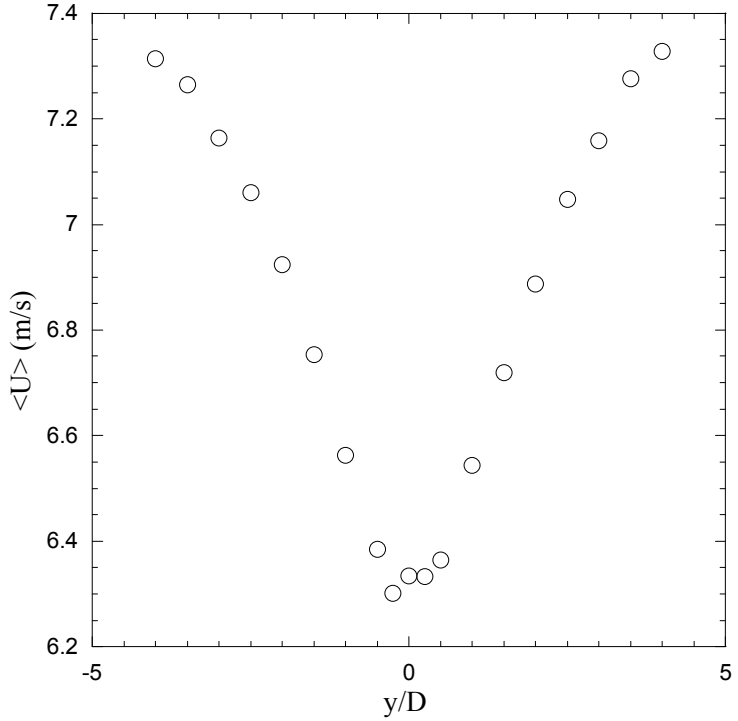

Figure 3.2: Mean velocity profile

To validate the velocity profile, (i) the velocity half-width (i.e., the value of *y/D* where the local mean velocity deficit is half the mean centerline velocity deficit), h ($=\sigma\sqrt{2\ln 2}$), and (ii) the centerline velocity to free-stream velocity ratio, U_c/U_∞, are compared to values from the literature. Table 3.2 shows the values of h and U_c/U_∞ found by Matsumura and Antonia (1993), Kang and Meneveau (2001), and Beaulac (2003) at different downstream positions (within the intermediate region of the wake) and Reynolds numbers, as well as the present results. The general trend that can be observed is that as *x/D* increases, h also increases. Likewise, increasing Re_D also seems to increase h. The value of *x/D* and Re_D in the present work fall within the values presented in table 3.2. Therefore, because the values of h and U_c/U_∞ also fall within the ranges of the previous work, it is reasonable to assume that the mean flows are consistent.

Reference	x/D	Re_D	h	U_c/U_∞
Matsumura and Antonia (1993)	10	5 830	0.81	0.91
	20		1.02	0.89
	40		1.49	0.91
Kang and Meneveau (2001)	25	75 600	1.66	0.76
Beaulac (2003)	53	16 200	2.40	0.86
Present work	40	24 260	1.80	0.86

Table 3.2: Values of h and U_c/U_∞ found in literature

Figure 3.3 presents the RMS profile of the velocity fluctuations for both velocity components (longitudinal and transverse). Symmetry about the y = 0 axis is observed. The highest fluctuations occur in the vicinity of the centre of the wake. This behaviour (including the small off-axis peaks in u_{RMS}) is consistent with previous measurements, including those of Beaulac (2003) and Matsumura and Antonia (1993).

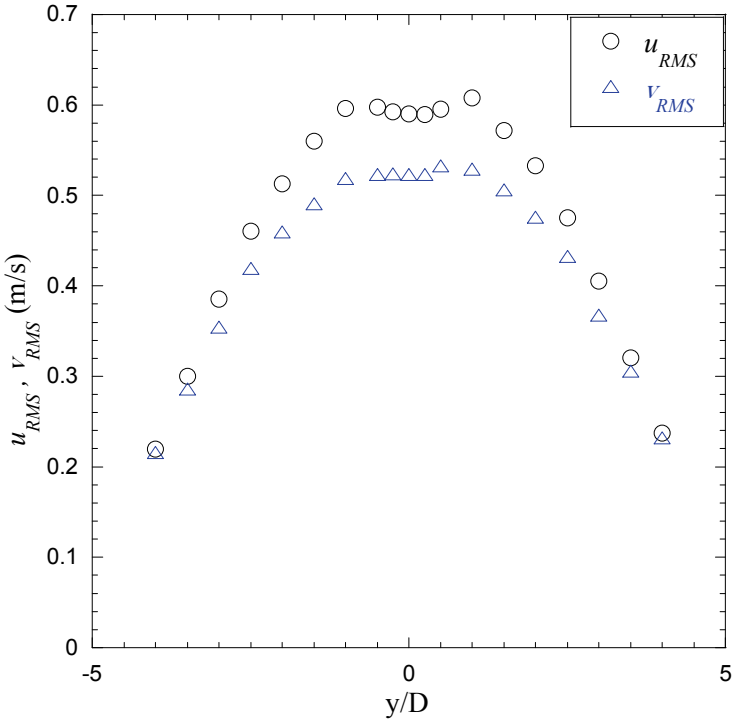

Figure 3.3: RMS profile for longitudinal and transverse velocity fluctuations

3.1.2.2 Two-Dimensionality of the Hydrodynamic Wake

Given the large aspect ratio of the cylinder (L/D = 16.5), the velocity field is expected to be two-dimensional (i.e., independent of the z-direction). This assumption was verified by Beaulac (2003), where a series of measurements were taken (in the same wind tunnel) at different axial positions and using a smaller cylinder diameter. The results from these measurements confirmed that the mean velocity profile and the RMS velocity profile, as well as the power spectral density of u were not affected by the axial position over the range $-3.5 \le z/D \le 3.5$. Given that the flow was shown to be homogeneous in the z-direction for a range of 7 cylinder diameters, and since the cylinder spans 16.5 diameters herein, it can be reasonably assumed that the hydrodynamic wake is two-dimensional at the plane of symmetry ($z/D = 0$) where all measurements were made.

3.1.3 Influence of the mandoline on the flow

As mentioned in Chapter 2, the mandoline's wire diameter was chosen to avoid the shedding of vortices. Using the free-stream velocity to get an upper bound, $\mathrm{Re}_{d_{wire}} = U_\infty d_{wire}/\nu = 34$, which is less than the critical value of $\mathrm{Re}_{d_{wire}} = 40$, at which vortices are shed (Lienhard and Lienhard, 2008). To verify whether the mandoline has an influence on the entire range of length scales, the power spectra of u with and without the mandoline at the centerline are shown in figure 3.4. Note that the mandoline has a negligible effect on the power spectra of the transverse component of velocity (not shown). From the power spectra of u with the mandoline, no vortex shedding frequency by the mandoline wires is observed. Comparing both spectra, the mandoline only appears to slightly affect the largest scales. The effect of this

difference can be quantified by comparing the flow parameters (u_{RMS}, v_{RMS}, S_u, S_v, K_u, K_v) with and without the presence of the mandoline. The u_{RMS} and v_{RMS} values are slightly greater for the wake with the mandoline. The largest difference (about 3 % relative difference) is at the centerline where u_{RMS} = 0.609 m/s in the presence of the mandoline, and u_{RMS} = 0.590 m/s without it. S_u, S_v, K_u and K_v remain unchanged and are thus unaffected by the mandoline's presence.

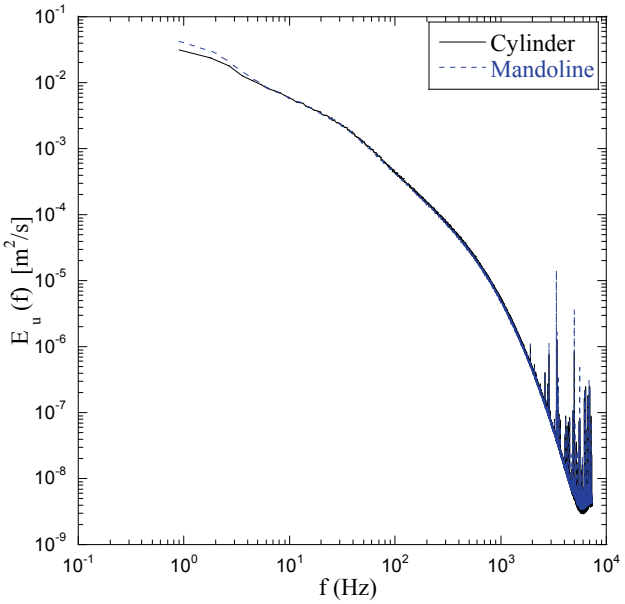

Figure 3.4: Influence of the mandoline on the power spectrum of *u* at the centerline

Furthermore, to ensure that the excitation of the mandoline wires does not reach a level that disrupts the flow, the resonance frequency of the mandoline (f_m) must be much larger than the cylinder's vortex shedding frequency (f_v). Beaulac (2003) estimated f_m to be 1 kHz, which also holds for to the mandoline in the present work (because the same wire diameter, length, and material were used), and f_v can be obtained from $S_t = f_v D/U_\infty = 0.21$. For $\mathrm{Re}_D = 32\,320$, f_v is 30 Hz. Hence, the

mandoline wires are unlikely to oscillate significantly with a vortex shedding frequency of about 30 Hz.

Based on the verifications presented in this section, the presence of the mandoline in the wake of the cylinder causes a slight perturbation to the velocity field.

3.2 The Thermal Field

3.2.1 Parameters of the Thermal Field

To describe the thermal field in the present work, the following parameters are calculated: (i) the mean temperature excess, $\overline{T} - T_\infty$ $(= \Delta\overline{T})$, (ii) θ_{RMS}, (iii) the skewness, S_θ, (iv) the kurtosis, K_θ, (v) the dissipation rate of the scalar variance, ε_θ, which is determined by assuming small-scale isotropy and using Taylor's frozen flow hypothesis:

$$\varepsilon_\theta = \frac{3\alpha}{\overline{U}^2}\overline{\left(\frac{d\theta}{dt}\right)^2}, \tag{3.4}$$

(vi) the integral length scale of the thermal field, ℓ_θ, which is determined in the same way as ℓ, (i.e., by evaluating the integral of the auto-correlation function up to its first zero), and (vii) the Kolmogorov scale for the scalar field, η_θ, which is defined as:

$$\eta_\theta = (\alpha^3 / \varepsilon)^{1/4}. \tag{3.5}$$

The temperature field parameters at the centerline are shown in table 3.3.

	Cylinder	Mandoline
Power input (kW)	1.5	1.1
$\overline{T} - T_\infty (^\circ\mathrm{C})$	0.68	0.50
$\theta_{RMS} (^\circ\mathrm{C})$	0.225	0.145
S_θ	0.315	-0.226
K_θ	3.41	3.06
ε_θ ($^\circ\mathrm{C}^2$/s)	0.174	0.0960
ℓ_θ (mm)	146.32	85.00
η_θ (mm)	0.25	

Table 3.3: Temperature field parameters at the centerline

In addition to the parameters discussed above, another important measure is the temperature power spectrum. This spectrum describes the distribution of the scalar variance per unit frequency from the largest eddies (integral scale), to the smallest eddies (Kolmogorov scale). Figure 3.5 shows this power spectrum for the case of the heated cylinder and the case of the heated mandoline. As expected it is observed that the majority of the contributions to the scalar variance come from the large (low-frequency) scales for both cases.

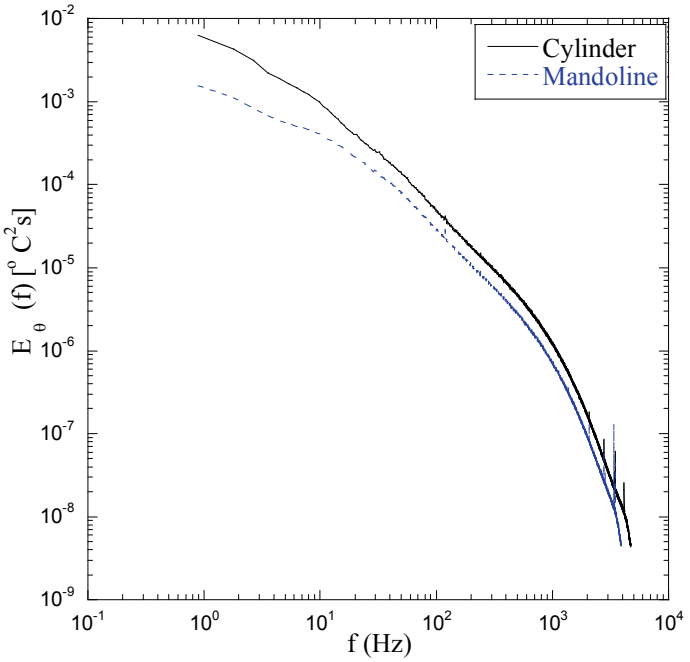

Figure 3.5: Power spectrum of θ at the centerline

3.2.2 Structure of the Thermal Wake

3.2.2.1 Symmetry of the Thermal Wake

Figure 3.6 plots the mean temperature excess, $\Delta T \left(= \overline{T} - T_{\infty}\right)$, profile for the wake heated by the cylinder and the mandoline. The mean temperature excess is measured (instead of $\overline{T}$) to eliminate the effects of drift in ambient room temperature during the experiment. This profile is theoretically predicted to be Gaussian (Pope, 2000) assuming self-similarity and a constant thermal diffusivity. The half-width of the mean temperature excess profile is slightly larger than the half-width of the mean velocity profile with a value of 2.62 diameters for the case of the heated cylinder and 2.52 diameters for the case of the heated mandoline. This is consistent with results from Rehab *et al.* (2001) who took measurements in the wake of a heated cylinder in a water tunnel, as well as those of Beaulac (2003).

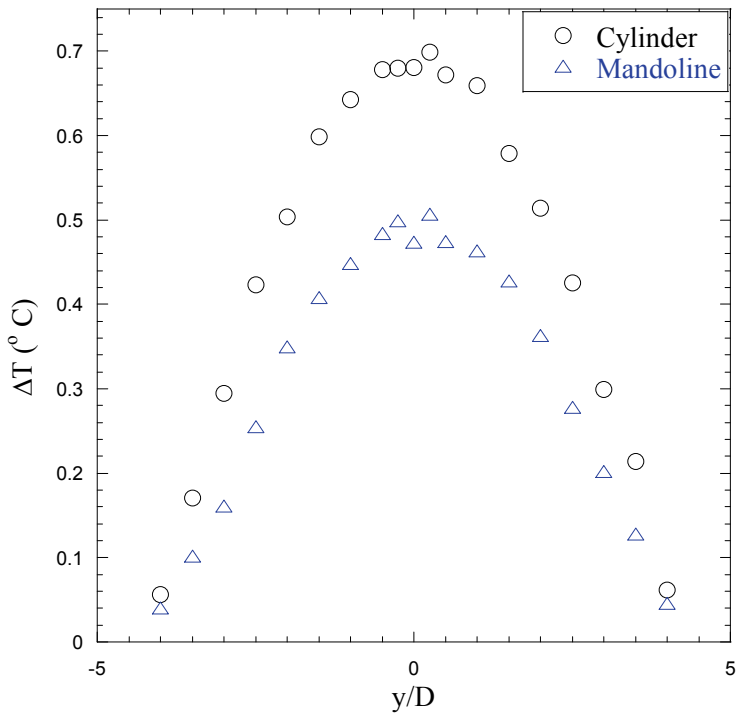

Figure 3.6: Mean temperature excess distribution for both scalar injection methods

Figure 3.7 plots the RMS profile of the temperature fluctuations for the two injection methods. The profile is distinctly (i) double-peaked, unlike that of the RMS velocity profiles, thus indicating the dynamics of the two fields are different, and (ii) the RMS differs from one injection mechanism to the other. It is, however, consistent with previous measurements, including those of Matsumura and Antonia (1993) and Beaulac (2003).

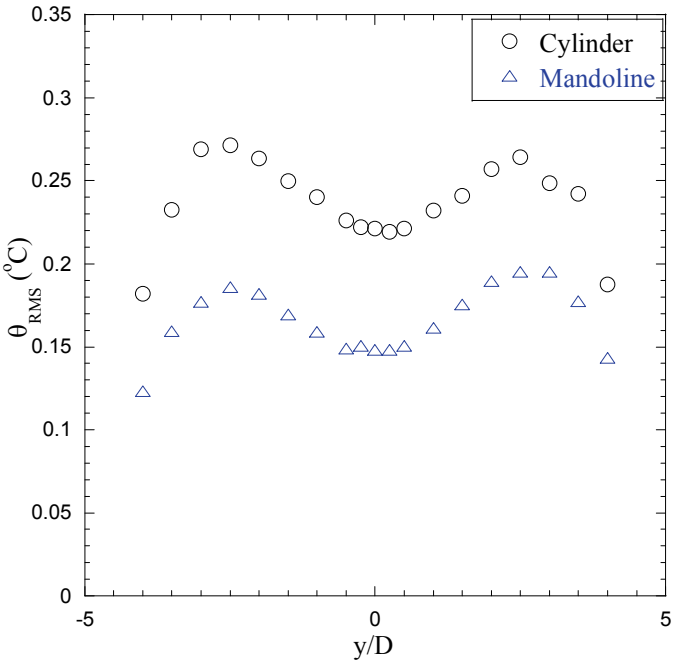

Figure 3.7: RMS profile of the temperature fluctuations

3.2.2.2 Two-Dimensionality of the Thermal Wake

Just like the hydrodynamic wake, given the large aspect ratio of the cylinder (L/D = 16.5), the thermal wake is expected to be two-dimensional (i.e., independent of the z-direction). Beaulac (2003) performed a series of temperature measurements (in the same wind tunnel) at different axial positions and using a smaller cylinder diameter. The results from these measurements confirmed that the temperature statistics were not affected by the axial position over the range $-3.5 \le z/D \le 3.5$.

Given that the thermal wake was shown to be homogeneous in the *z*-direction for a range of 7 cylinder diameters, and since the cylinder spans 16.5 diameters in this work, it can be reasonably assumed that the thermal wake created by heating the cylinder is two-dimensional at the plane of symmetry, $z/D = 0$, where all measurements were made.

3.2.3 Passivity of the Scalar

The scalar (temperature) was injected in one of two ways: (i) by heating the cylinder and (ii) by heating the mandoline placed downstream of the cylinder. The effect of the scalar field on the velocity field is quantified by (i) comparing turbulent statistics of the velocity field for the isothermal and heated cases, and (ii) comparing the ratio of the rate of buoyant production of the turbulent kinetic energy to its dissipation rate.

Table 3.4 presents flow parameters in the isothermal wake and heated wake. (The heated wake examined is the one heated by the cylinder because it has a higher temperature increase than that heated by the mandoline.) The differences in the flow parameters in the isothermal wake and heated wake are within experimental error, validating the passivity of the scalar field.

	x/D =40	
	isothermal wake	heated wake
u_{RMS} (m/s)	0.599	0.590
v_{RMS} (m/s)	0.525	0.523
S_u	0.014	0.099
S_v	-0.011	-0.006
K_u	2.79	2.81
K_v	2.75	2.79
ε (m^2/s^3)	2.37	2.48

Table 3.4: Flow parameters at the centerline in the isothermal and heated wake

To compare all the scales, the power spectrum of v (because it is the velocity fluctuation which is in the direction of the highest temperature gradient) in the isothermal wake and heated wake is shown in figure 3.8. The effect of temperature on the power spectrum of v is negligible.

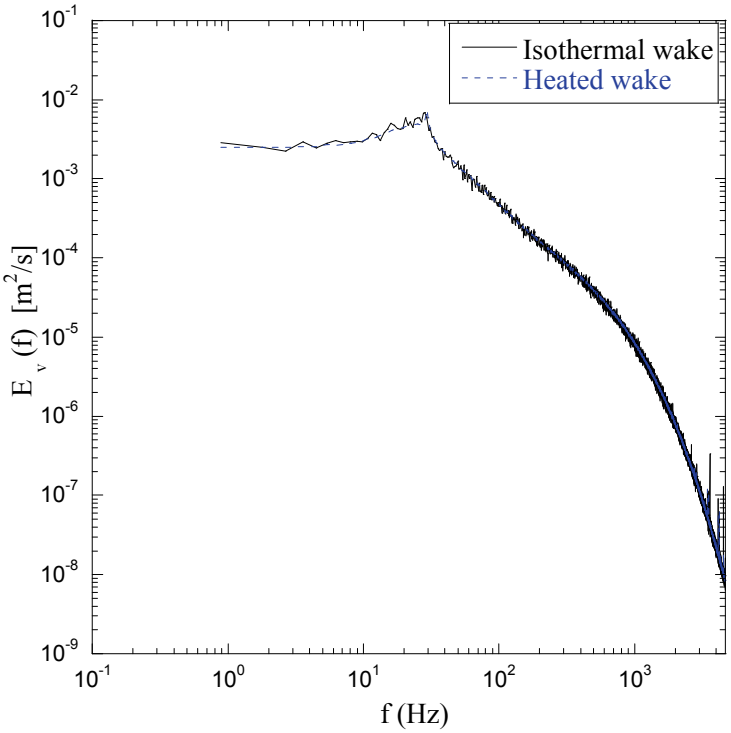

Figure 3.8: Effect of the scalar on the power spectrum of v

The second measure of the passivity of the scalar is estimating the ratio of the buoyant production of turbulent kinetic energy ($g_i \overline{u_i \theta} / \overline{T}$) to the dissipation of turbulent kinetic energy (ε). Calculating this ratio is difficult because the cylinder is placed vertically in the experiments and the temperature field is statistically homogeneous in the direction of the gravitational acceleration vector (which means that $g_i \overline{u_i \theta} = 0$). As a worst-case approximation, this quantity can be estimated if the cylinder were rotated 90° so that the direction of the gravitational acceleration is assumed to be in the transverse direction. In that case, the ratio would be:

$$\frac{\text{Buoyant production of turbulent kinetic energy}}{\text{Dissipation of turbulent kinetic energy}} = \frac{\left(g\,\overline{v\theta}/\overline{T}\right)}{\varepsilon} \tag{3.6}$$

The highest ratio from the different configurations is 1.88% (x/D = 40, y/D = 2.5, heated cylinder) which shows that buoyancy has a small effect on the flow and the scalar field can be assumed to be passive.

Chapter 4: Results and Discussion

Measurements (and a related discussion) of Pr_T and r are presented in sections 4.1 and 4.2, respectively, for the two scalar fields under consideration herein. These results include a description of how these two quantities were calculated, followed by a comparison of different scalar injection methods. Furthermore, the sensitivity of Pr_T and r to the changes in scalar injection methods is discussed. For completeness, an error and uncertainty analysis is presented in Appendix A for the temperature (A.1.1) and velocity (A.1.2) measurements individually. Lastly, an uncertainty analysis for Pr_T and r follows in sub-section A.1.3.

4.1 The Turbulent Prandtl Number

To calculate Pr_T, the following four quantities need to be determined:

(i) the mean velocity gradient, $\partial\overline{U}/\partial y$,

(ii) the mean temperature gradient, $\partial\overline{T}/\partial y$,

(iii) the turbulent Reynolds stress, $\overline{uv}$, and

(iv) the transverse turbulent heat flux, $\overline{v\theta}$.

Once these four quantities are known, Pr_T can be calculated from the following:

$$\mathrm{Pr}_T \equiv \frac{\nu_T}{\alpha_T} = \frac{-\overline{uv}/\dfrac{\partial\overline{U}}{\partial y}}{-\overline{v\theta}/\dfrac{\partial\overline{T}}{\partial y}}. \tag{4.1}$$

To determine the mean velocity gradient, $\partial\overline{U}/\partial y$, a Gaussian curve is least-squares fitted to the longitudinal mean velocity profile (shown in figure 4.1) of the form presented in Chapter 3:

$$\overline{U} = A - Be^{\frac{-(y/D-y_o/D)^2}{2\sigma^2}}. \tag{4.2}$$

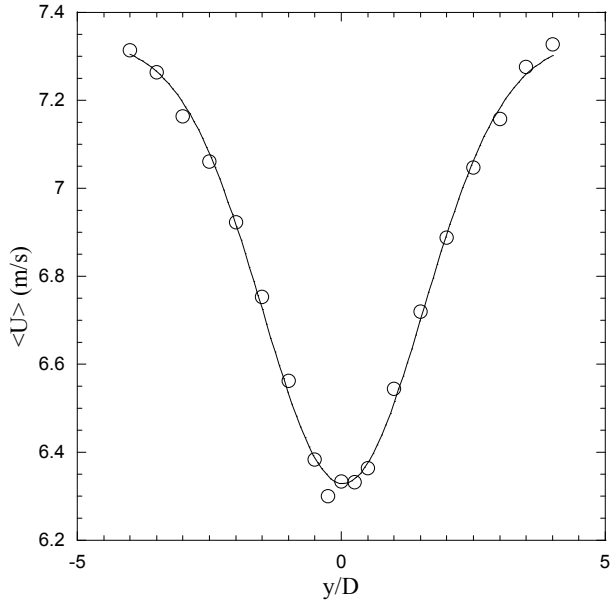

Figure 4.1: Longitudinal mean velocity profile with a Gaussian curve-fit

To determine $\partial\overline{T}/\partial y$, a 6th order polynomial with only even terms (to guarantee even symmetry in the *y*-direction) is least-squares fitted to the mean temperature excess profiles (as shown in figure 4.2):

$$\Delta\overline{T} = c_1 + c_2(y/D - y_o/D)^2 + c_3(y/D - y_o/D)^4 + c_4(y/D - y_o/D)^6. \tag{4.3}$$

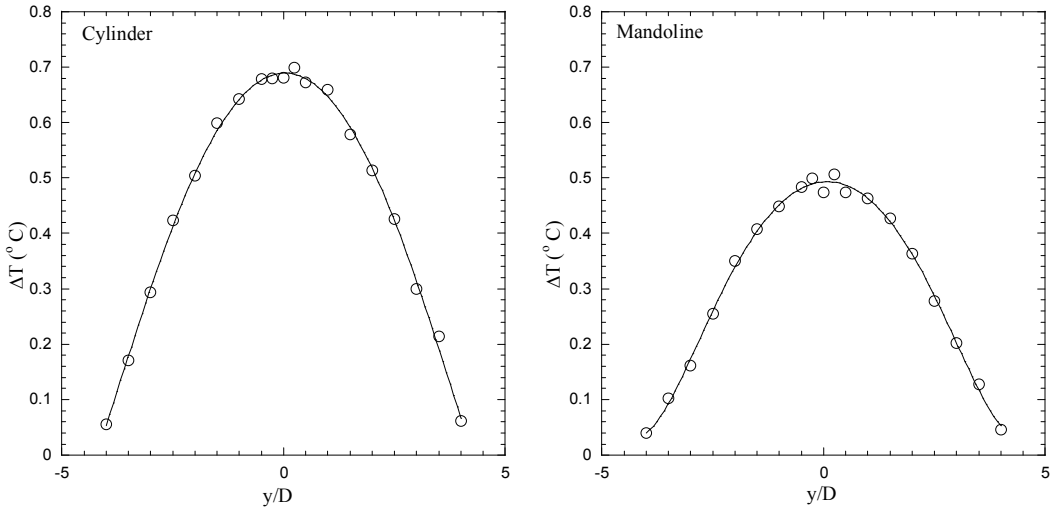

Figure 4.2: Mean temperature excess profiles with a 6th order polynomial curve-fit

The third quantity used to calculate Pr_T is the turbulent Reynolds stress, $\overline{uv}$, defined as the mean of the product of the longitudinal and transverse velocity fluctuations. $\overline{uv}$ quantifies the average *x*-momentum transfer in the *y*-direction due to the turbulent eddies. Because of the underlying symmetries of the flow, the profile is expected to be antisymmetric in the *y*-direction. However, due to a slight yaw offset in either (i) the calibration, or (ii) the installation of the X-probe (in the wind tunnel), the measured $\overline{uv}$ data did not exactly exhibit this symmetry. Therefore, to account for this yaw offset, a correction was made to the effective angles of each hot-wire. A value of 1.5° was heuristically determined to account for this offset. Note that this correction only affected the $\overline{uv}$ results. The uncorrected and corrected $\overline{uv}$ distributions are shown in figure 4.3. In this flow, the peaks roughly occur at the location of highest production, i.e. where $\partial\overline{U}/\partial y$ is the largest ($y/D \approx \pm 1.5$).

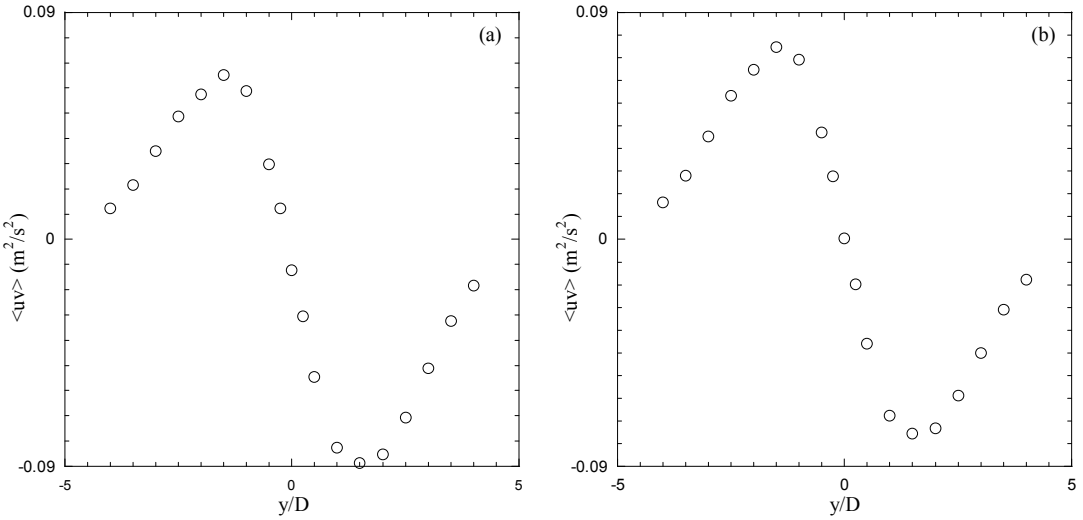

Figure 4.3: (a) Uncorrected turbulent Reynolds stress distribution, (b) Corrected turbulent Reynolds stress distribution

The fourth and final quantity necessary to calculate Pr_T is the transverse turbulent heat flux, $\overline{v\theta}$, plotted in figure 4.4 for both passive scalar fields. It quantifies how the velocity fluctuations in the transverse direction transport the scalar. As with $\overline{uv}$, the profile must also be antisymmetric in the *y*-direction, due to the underlying symmetries of the flow.

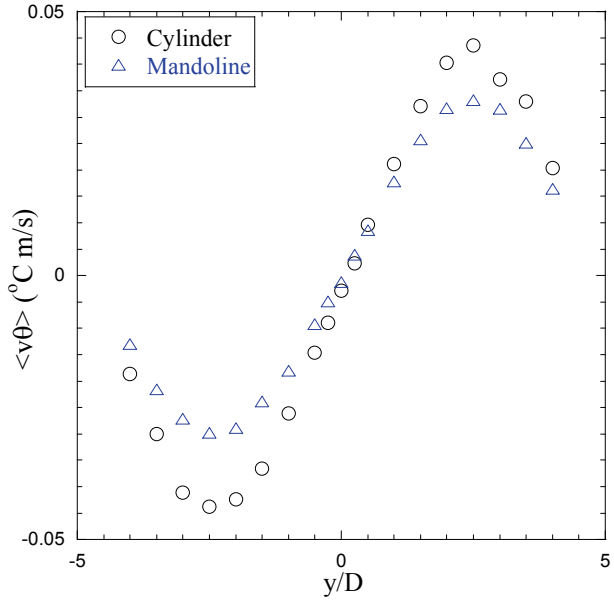

Figure 4.4: Transverse turbulent heat flux distribution for the two scalar fields

Having presented all four quantities needed to calculate Pr_T, figure 4.5 plots the resulting distributions of Pr_T for each scalar field. Given the symmetries of the quantities used in calculating Pr_T, it must exhibit even symmetry in the *y*-direction. As with any experiment, the measurement uncertainties rendered the actual distribution of Pr_T slightly asymmetric. Given that (i) Pr_T must exhibit even symmetry in *y*, and (ii) any component that is odd in *y* must not be physical in origin, only the even component of the measured results is presented (by averaging data points on either side of the $y = 0$ line of symmetry).

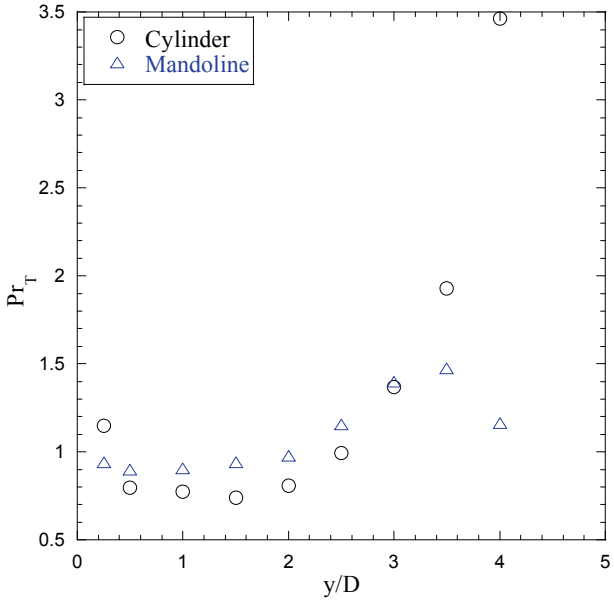

Figure 4.5: Distribution of the turbulent Prandtl number for both scalar fields

Looking at figure 4.5, Pr_T is found to vary across the wake for both scalar field injection methods. For the case of the heated cylinder, the minimum value of Pr_T is 0.74, and the maximum is 3.5 (near the edge of the wake). The minimum value of Pr_T for the case of the mandoline is 0.90 and the maximum is 1.5. Note that the value at the centerline is indeterminate because all four quantities needed to calculate

Pr_T are zero there; hence Pr_T is not plotted at the centerline. A comparison of Pr_T values for the two scalar fields shows that, for the majority of the wake (y/D = 0.5 to 3), Pr_T for the case of the mandoline is greater than Pr_T for the case of the heated cylinder, with a largest absolute difference of 0.2. On the other hand, Pr_T using a heated cylinder is higher near the edge of the wake and close to the center with the largest difference (of 2.3) at y/D = 4. The large difference near the edge of the wake is due to the larger mean temperature gradient for the heated cylinder at that location. The resulting discrepancy at the edge of the wake is an artifact of the curve-fit at that location, which overestimates the temperature gradient there. This discrepancy occurs because it is the last point and therefore does not account for the flattening of the profile as it approaches zero for larger values of y. Consequently, the difference in Pr_T between the two scalar fields at y/D = 4 is overestimated.

As discussed in Chapter 1, the typical Pr_T value used in the modeling of turbulent passive scalars for free shear flows is 0.7. However, the experimental results shown above contradict this generalization because: (i) the value of Pr_T is not uniformly distributed across the wake, (ii) the average Pr_T value is not 0.7 for either scalar field case, and most importantly (iii) Pr_T depends upon the scalar injection method (for the identical turbulent flow). Therefore, modellers who take into account changes in the type of flow (e.g., bounded vs. free shear flow) when modeling the scalar field, should also factor in the injection method of the scalar.

4.2 The Mechanical-to-Thermal Time-Scale Ratio

To calculate the mechanical-to-thermal time-scale ratio, one requires:

(i) the turbulent kinetic energy, *k*,

(ii) the dissipation of turbulent kinetic energy, ε,

(iii) the scalar variance, k_θ, and

(iv) the dissipation of the scalar variance, ε_θ:

$$r \equiv \frac{k/\varepsilon}{k_\theta/\varepsilon_\theta}. \tag{4.4}$$

The turbulent kinetic energy, *k*, is calculated from the following definition:

$$k \equiv \frac{1}{2}\overline{u_i u_i} = \frac{1}{2}\left(\overline{u^2} + \overline{v^2} + \overline{w^2}\right), \tag{4.5}$$

where $\overline{w^2}$ was determined from measurements with the X-probe rotated by 90°. The dissipation of turbulent kinetic energy, ε, is:

$$\varepsilon = \frac{15\nu}{\overline{U}^2}\left[\overline{\left(\frac{du}{dt}\right)^2}\right]. \tag{4.6}$$

The scalar variance, k_θ, is defined as:

$$k_\theta \equiv \frac{1}{2}\overline{\theta^2}, \tag{4.7}$$

And the dissipation of the scalar variance, ε_θ, is determined from:

$$\varepsilon_\theta = \frac{3\alpha}{\overline{U}^2}\overline{\left(\frac{d\theta}{dt}\right)^2}. \tag{4.8}$$

To obtain the time derivatives of *u* and θ, the "spectral" data sets were used because their sampling rate respected the Nyquist criterion. Thus, numerical derivatives could be computed directly from the acquired data. Also, note that due to the underlying

symmetries, *r* is expected to be symmetric about the centerline. Hence, only one half of the wake is plotted in figure 4.6.

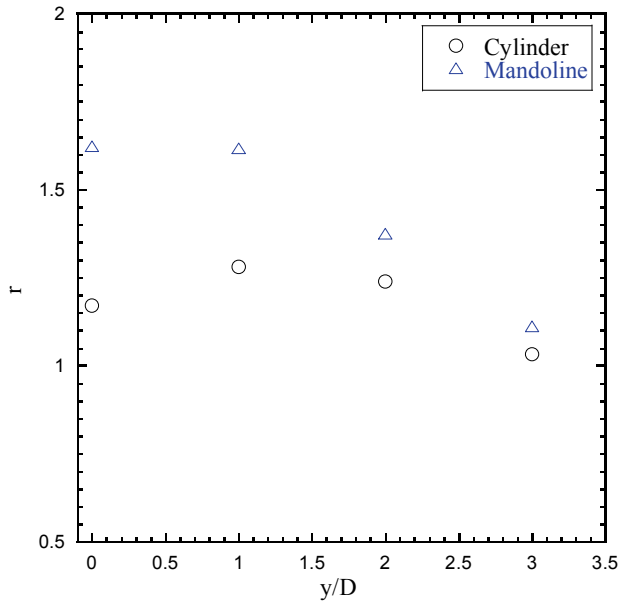

Figure 4.6: The mechanical-to-thermal time-scale ratio distribution

As shown in figure 4.6, the values of *r* vary across the wake for both scalar fields. For the case of the flow heated by the cylinder, the highest value is 1.28 and the lowest is 1.03. For the case of the flow heated by the mandoline, the highest value is 1.62 and the lowest is 1.11. Overall, *r* for the scalar field created by the mandoline is higher than for the case of the heated cylinder. The largest difference in *r* exists at the centerline (0.45) and the smallest (0.08) occurs near the edge of the wake.

Typically, *r* is assumed to be constant in turbulence models with a value of 2 for free shear flows (determined from experimental *r* results which ranged from 1.5 to 2.5). However, in this work *r* is not constant but varies throughout the wake, with an average value of 1.21 for the case of the heated cylinder, and 1.43 for the case of the mandoline. Even for these two cases, considerable differences exist in *r*. As discussed in section 3.2, these two scalar injection methods do not affect the flow (velocity

field). To date, it has been assumed that the mechanical-to-thermal time-scale ratio is not affected when changing only the scalar injection method. However, as shown by the measured data, changes in scalar injection can lead to significant changes in r (up to an absolute difference of 0.45). Hence, like Pr_T, r not only depends on the type of flow, but on the scalar field injection as well.

Chapter 5: Conclusions and Future Work

5.1 Summary and Conclusions

The majority of engineering flows are turbulent, and rapidly mix mass, momentum and energy. Prediction of these flows is important, but remains difficult given the non-linear and chaotic nature of turbulence. To overcome this impediment, turbulence models are applied to simplify the governing equations. The present work dealt with the mixing of passive scalars (i.e., small temperature differences) in a turbulent flow. When modeling turbulent passive scalars, the turbulent Prandtl number (Pr_T) and the mechanical-to-thermal time-scale ratio (r) are two important and recurring quantities. They are determined from experiments and generally assumed to be constant. Furthermore, modellers often change the value of this constant based on the type of turbulent flow under consideration. For example, for turbulent shear flows, the generally employed values of Pr_T and r are constant and given as 0.7 and 2, respectively.

The objective of the work was to study the sensitivity of Pr_T and r to changes in scalar field initial conditions within the same turbulent flow. The turbulent wake of a circular cylinder was chosen with the scalar field injected either by heating the cylinder or by heating an array of fine parallel wires (called a mandoline) placed downstream of the cylinder.

The experiments were performed in a wind tunnel where simultaneous velocity-temperature measurements, using hot-wire anemometry and cold-wire

thermometry, were made. The cylinder (an aluminum tube of circular cross-section with a heating element on the inside) was placed at the entrance of the test section and used to generate the turbulent wake. When the flow was not heated by the cylinder, it was heated by the mandoline, which was made of 13 fine wires and was placed 10 cylinder diameters downstream of the cylinder's center. The sensors were placed at 40 diameters downstream of the cylinder's axis and the measurements were made across the wake in the transverse (y) direction.

Flow characteristics were presented and the symmetry and two-dimensionality of both the hydrodynamic wake and the thermal wake were discussed. Furthermore, the influence of the mandoline on the flow was shown to be acceptably small and the passive nature of the scalar was confirmed.

By means of simultaneous velocity-temperature measurements, Pr_T and r were calculated for the two scalar fields under consideration. The results demonstrated that the value of Pr_T is not constant throughout the wake for either scalar field. In fact, the typical value of 0.7 used in turbulence models underestimated the values calculated in the present work. Likewise, the values of r varied across the wake for both scalar fields. Furthermore, the typical modeling value of 2 overestimated r for both scalar injection cases. Most importantly, both these quantities varied with different scalar injection methods, despite being within the same flow. Therefore, not only does the type of flow play a role in determining these quantities, but so does the scalar injection method. This dependence should be taken into account in turbulence models.

5.2 Suggestions for Future Work

Future work would include sensitivity tests of CFD simulations to the variations in Pr_T and r found in this work. These tests would compare mean temperature and scalar variances as obtained with the typical modeling values and those from this work. Such tests would identify and quantify how inaccuracies in these quantities directly affect the outputs of interest (i.e., the mean scalar field and scalar variance).

Further experimental investigations could also be performed by varying different flow parameters such as the type of flow, the Reynolds number, the downstream location, etc. to study the sensitivity of Pr_T and r to different scalar injection methods for different flow conditions. The overall goal would be to better understand and quantify the sensitivity of these two quantities for various parameters. These future investigations could help develop improved models to accurately predict the distribution of Pr_T and r.

A practical extension of this study would be for turbulent jets, a flow widely used in engineering applications (e.g., combustion), where the initial conditions can vary significantly. It has been shown that the velocity field in jets depends on the initial conditions (e.g., a "top-hat" velocity profile at the jet exit vs. a fully-developed one) for downstream distances up to $x/D = 30$ (Antonia and Zhao, 2001). Analogously, one might expect that the scalar field statistics would also depend on their initial conditions at the jet exit. Consequently, so should Pr_T and r, and the effect of the scalar field initial conditions in this flow will play an important role in

the scalar field evolution, at least for intermediate downstream distances, which are relevant to many, if not most, engineering applications.

References

Antonia, R.A. & Browne, L.W.B. (1987). Conventional and conditional Prandtl number in a turbulent plane wake. *International Journal of Heat and Mass Transfer*, **30**(10), 2023-2030.

Antonia, R.A. & Zhao, Q. (2001). Effect of initial conditions on a circular jet. *Experiments in Fluids*, **31**(3), 319-323.

Antonia, R.A., Zhou, Y, & Matsumura, M. (1993). Spectral characteristics of momentum and heat-transfer in the turbulent wake of a circular-cylinder. *Experimental Thermal and Fluid Science*, **6**(4), 371-375.

Beaulac, S. (2003) The Effect of the injection scale on scalar mixing in the turbulent wake of a circular cylinder. M Eng thesis, McGill University.

Beaulac, S., & Mydlarski, L. (2004). Dependence on the initial conditions of scalar mixing in the turbulent wake of a circular cylinder. *Physics of Fluids*, **16**(8), 3161-3172.

Béguier, C., Dekeyser, I. & Launder, B. (1978). Ratio of scalar and velocity dissipation time scales in shear-flow turbulence. *Physics of Fluids*, **21**(3), 307-310.

Browne, L.W.B. & Antonia, R. (1983). Measurements of turbulent Prandtl number in a plane jet. *Journal of Heat Transfer*, **105**(3), 663-665.

Browne, L.W.B. & Antonia, R. (1987). The effect of wire length on temperature statistics in a turbulent wake. *Experiments in Fluids*, **5**(6), 426-428.

Browne, L.W.B., Antonia, R.A. & Chua, L.P. (1989). Calibration of X-probes for turbulent-flow measurements. *Experiments in Fluids*, **7**(3), 201-208.

Bruun, H.H. (1995). *Hot-Wire Anemometry: Principles and Signal Analysis*, Oxford University Press.

Bunker, A.F. (1956). Measurements of counter-gradient heat flows in the atmosphere. *Australian Journal of Physics*, **9**, 133-143.

Chambers, A., Antonia, R.A., & Fulachier, L. (1985). Turbulent Prandtl number and spectral characteristics of a turbulent mixing layer. *International Journal of Heat and Mass Transfer*, **28**(8), 1461-1468.

Chang, K. & Cowen, E. (2002). Turbulent Prandtl number in neutrally buoyant turbulent round jet. *Journal of Engineering Mechanics*, **128**(10), 1082-1087.

Chua, L. & Antonia, R. (1990). Turbulent Prandtl number in a circular jet. *International Journal of Heat and Mass Transfer*, **33**(2), 331-339.

Comte-Bellot, G. & Corrsin, S. (1971). Simple Eulerian time correlation of full- And narrow-band velocity signals in grid-generated, isotropic turbulence. *Journal of Fluid Mechanics*, **48**, 273-337.

Dimotakis, P. (2005). Turbulent mixing. *Annual Review of Fluid Mechanics*, **37**, 329-356.

Durbin, P. (1982). Analysis of the decay of temperature-fluctuations in isotropic turbulence. *Physics of Fluids*, **25**(8), 1328-1332.

Jørgensen, F.E. (2002). How to measure turbulence with hot-wire anemometers. Dantec Dynamics publication.

Kang, H. & Meneveau, C. (2001). Passive scalar anisotropy in a heated turbulent wake: New observations and implications for large-eddy simulations. *Journal of Fluid Mechanics*, **442**, 161-170.

Kays, W.M. (1994). Turbulent Prandtl number – Where are we? *Journal of Heat Transfer*, **116**, 284-295.

Kovásznay, L. (1949). Hot-wire investigation of the wake behind cylinders at low Reynolds numbers. *Proceedings of the Royal Society of London*. Series A, Mathematical and Physical Sciences, **198**(1053), 174-190.

Launder, B.E. (1975). Progress in the modelling of turbulent transport. *Von Karman Institute for Fluid Dynamics* – Lecture Series 76: Prediction methods for turbulent flows.

Launder, B.E. (1976). Heat and Mass transport. *Topics in Applied Physics: Turbulence*. Springer-Verlag Berlin Heidelberg New York.

Lemay, J. (2007). Notice d'utilisation des anémomètres à courant constant, *Private Communication.*

Lemay, J. & Benaïssa, A. (2001). Improvement of cold-wire response for measurements of temperature dissipation, *Experiments in Fluids*, **31**, 347-356.

Lienhard, J. H. (1988). The Decay of Turbulence in Thermally Stratified Flow, PhD dissertation, University of California at San Diego.

Lienhard IV J.H. & Lienhard V J.H. (2008). *A Heat Transfer Textbook*, Phlogiston Press.

Matsumura, M. &Antonia, R. A. (1993). Momentum and heat transport in the turbulent intermediate wake of a circular cylinder, *Journal of Fluid Mechanics*, **250**, 651-668.

Mydlarski, L. & Warhaft, Z. (1998). Passive scalar statistics in high-Péclet-number grid turbulence. *Journal of Fluid Mechanics*, **358**, 135-175.

Pope, S. B. (2000) *Turbulent Flows*, Cambridge University Press.

Rehab, H., Antonia, R. A. & Djendji, L. (2001). Streamwise evolution of a high-Schmidt number passive scalar in a turbulent plane wake, *Experiments in fluids*, **31**, 186-192.

Schiestel, R. (2008). *Modeling and Simulation of Turbulent Flows*, ISTE and Wiley.

Shraiman, B., & Siggia, E. (2000). Scalar turbulence. *Nature*, **405**(6787), 639-646.

Sreenivasan, K. (1991). On local isotropy of passive scalars in turbulent shear flows. Proceedings. *Mathematical, Physical, and Engineering Sciences*, **434**(1890), 165-182.

Sreenivasan, K., Tavoularis, S., Henry, R., & Corrsin, S. (1980). Temperature-fluctuations and scales in grid-generated turbulence. *Journal of Fluid Mechanics*, **100**, 597-621.

Tavoularis, S. & Corrsin, S. (1981). Experiments in nearly homogenous turbulent shear-flow with a uniform mean temperature-gradient .1. *Journal of Fluid Mechanics*, **104**, 311-347.

Taylor, J.R. (1997). *An Introduction to Error Analysis: The Study of Uncertainties in Physical Measurements*, University Science Books.

Tennekes, H. & Lumley, J. L. (1972). *A First Course in Turbulence*. MIT Press.

Warhaft, Z. (1980). An experimental-study of the effect of uniform strain on thermal fluctuations in grid-generated turbulence. *Journal of Fluid Mechanics*, **99**, 545-573.

Warhaft, Z. (2000). Passive scalars in turbulent flows. *Annual Review of Fluid Mechanics*, **32**, 203-240.

Warhaft, Z. & Lumley, J. (1978). Experimental-study of decay of temperature-fluctuations in grid-generated turbulence. *Journal of Fluid Mechanics*, **88**, 659-684.

Wilcox, D.C. (1993). *Turbulence Modeling for CFD*, DCW Industries, Inc.

Appendix A

A.1 Sources of Error and Uncertainty Analysis

In this section, an uncertainty analysis is performed for the temperature (A.1.1) and velocity (A.1.2) measurements individually, followed by the uncertainties in the results of Pr_T and r (A.1.3). A combination of uncertainty analysis models from both Taylor (1997) and Jørgensen (2002) is used to calculate the total relative expanded uncertainty at a given confidence level. This model involves calculating the relative standard uncertainties from each source of error which can affect the measurement. Then, the contributions from each error are combined using a propagation of uncertainties and a coverage factor of 2 to obtain a confidence level of 95 %.

A.1.1 Uncertainty in the Temperature Measurements

Constant current anemometer

The sources of error which can occur in constant current anemometry can be due to (i) sensitivity to velocity changes, (ii) electronic noise, and (iii) limitations in the frequency response. The current is selected such that the sensor's sensitivity to velocity changes is small and a good signal-to-noise ratio is obtained. Secondly, electronic noise is negligible (compared to other sources of error) given the large signal-to-noise ratio in this flow. Lastly, the frequency response is an issue only for small scale measurements, as explained in Chapter 2. In this work, large-scale

quantities are considered; hence the frequency response is a non-issue. Therefore, the sources of error for the temperature measurements are deemed negligible.

Calibration and curve-fit

When calibrating the cold-wire (as described in 2.5.1), the largest source of error is the temperature read-out from the thermocouple, which has a resolution of ±0.1°C. This error is conservatively assumed to have a uniform distribution, meaning that it is equally likely that the measured values lie within the given interval. The standard deviation for this uniform distribution is $0.1/\sqrt{3}$. Thus, the relative standard uncertainty is calculated from:

$$uncertainty = \frac{1}{\sqrt{3}}\left(\frac{0.1}{T}\right)\times 100\%, \tag{A.1}$$

where T is the nominal value of the temperature read by the thermocouple. Taking the smallest value read (to obtain the largest relative uncertainty from the calibration), the relative standard uncertainty is 0.24 %.

Furthermore, the curve-fit to the calibration data (E vs. T) causes an uncertainty which is calculated by taking the standard deviation of the curve-fitting errors. The curve-fitting errors are calculated by subtracting the measured temperature ($T_{i,measured}$) from the temperature evaluated by the curve-fit at that same voltage ($T_{curve-fit}(E_i)$). This difference is divided by $T_{curve-fit}(E_i)$ to obtain a relative error. This measure of error assumes that the output voltages (E_i) have negligible uncertainty, which is reasonable considering the comments mentioned previously for the anemometer. To obtain a value of the standard deviation, these errors are squared, summed, and divided by the number of data points minus two (N-2). (The minus two

is a consequence of having used two degrees of freedom to obtain the coefficients of the least-squares fit line.) Hence, the following relationship returns the relative standard uncertainty caused by the linear least-squares fit:

$$uncertainty = \sqrt{\frac{1}{N-2}\sum_{i=1}^{N}\left(\frac{T_{curve-fit}(E_i) - T_{i,measured}}{T_{curve-fit}(E_i)}\right)^2} \times 100\,\%\,. \qquad \text{(A.2)}$$

In this work, the relative standard uncertainty is found to be 0.22 %.

DAQ board resolution

The resolution uncertainty of the data acquisition board is random with a uniform distribution. That being said, the relative standard uncertainty is determined from the following expression (Jørgensen, 2002):

$$uncertainty = \left(\frac{1}{\sqrt{3}}\frac{1}{T}\frac{\partial T}{\partial E}\frac{E_{DAQ}}{2^n}\right)\times 100\%\,, \qquad \text{(A.3)}$$

where T is taken as the lowest temperature value recorded, $\partial T / \partial E$ is the slope of the calibration curve (1.4), E_{DAQ} is the voltage span used to acquire the data (10 V) and n is the number of bits (16) of the acquisition system. Thus, the relative standard uncertainty is 0.0005 %.

Ambient condition variations

Ambient variations in temperature and pressure cause drifts in the free-stream temperature over the course of an experiment. These variations only affect mean temperature measurements and not the fluctuating component. Since the fluctuating signal is high-pass filtered, errors from drifts in the room temperature (which occur at frequencies lower than the high-pass frequency) are eliminated. Therefore, to account for the drifts, the free-stream temperature is measured and subtracted from the mean

temperature measurements, thus obtaining the mean temperature excess. The uncertainties in measurements of the mean temperature excess are discussed in sub-section A.1.3 as they affect Pr_T.

Probe positioning

Since the resistance of the cold-wire changes with temperature and does not depend on the direction of the flow, minor misalignments of the probe will not have any effect on the uncertainty of the temperature measurements (unlike the velocity probe, which will be discussed in A.1.2). Instead, the uncertainty will be in the value of its corresponding position (*y/D*).

Total expanded uncertainty for the temperature measurements

All the uncertainties mentioned above are summarized in table A.1 in order of decreasing importance.

Sources of error	Relative standard uncertainty
Calibration	0.24 %
Calibration curve-fit	0.22 %
DAQ board resolution	0.0005 %
Anemometer	negligible
Probe positioning	negligible

Table A.1: The uncertainties in the temperature measurements

To calculate the total expanded uncertainty, the following formula is used with a coverage factor of 2 to assure a 95 % confidence level in the uncertainty:

$$\textit{Total uncertainty} = 2\sqrt{(\text{uncertainty}_1)^2 + (\text{uncertainty}_2)^2 + (\text{uncertainty}_3)^2 + \ldots}\,. \quad \text{(A.4)}$$

Therefore, substituting the values of table A.1 into equation A.4 results in a total expanded uncertainty of **0.65%**.

A.1.2 Uncertainty in the Velocity Measurements

Constant temperature anemometer

The constant temperature anemometer has low drift, low noise, and good repeatability. The frequency response, as discussed in Chapter 2, is not an issue since the cut-off frequency of the anemometer is much greater than the highest frequencies encountered in the flow. Therefore, the uncertainty in velocity measurements caused by the anemometer is taken to be negligible comparing to the other sources of error.

Calibration equipment and curve-fit

The calibration equipment causes a relative uncertainty of 1%. This is a typical value for commercial calibrators and is based on the standard deviation of a random normal distribution error (Jørgensen, 2002).

The curve-fit to the calibration data (E^2 vs U) causes an uncertainty which is calculated by taking the standard deviation of the curve-fitting errors. Also, since the calibration is performed for varying temperature, there is a correction made to the calibration constants A and B (equations 2.4 and 2.5, in Chapter 2). This correction involves fitting equations 2.4 and 2.5 to the A vs. T and B vs. T data, respectively. These curve-fits also cause uncertainties in the velocity measurements and must be considered. However, unlike the calibration curve-fit for temperature measurements, both the dependent and independent variables are subject to uncertainties.

To calculate the uncertainty due to the calibration curve-fits to E^2 vs U, A vs. T, and B vs. T, the following equation is used:

$$uncertainty = \sqrt{\underbrace{\frac{1}{N-3}\sum_{i=1}^{N}\left(\frac{U_{curve-fit}(E_i)-U_{i,measured}}{U_{curve-fit}(E_i)}\right)^2}_{1} + \underbrace{\left(\frac{1}{U}\frac{\partial U}{\partial A}\sigma_A\right)^2}_{2} + \underbrace{\left(\frac{1}{U}\frac{\partial U}{\partial B}\sigma_B\right)^2}_{3}} \times 100\%, \tag{A.5}$$

where term 1 is similar to the equation A.2. The minus three results from having used three degrees of freedom to determine the calibration coefficients A, B and n from equation 2.3. Terms 2 and 3 account for the uncertainty in A and B, respectively and are added in quadrature following the propagation of uncertainties theory presented by Taylor (1997). Because both A (or B) and T have uncertainties, the equivalent uncertainty in A (or B) must be obtained (as discussed in Taylor, 1997). Thus, σ_A (from term 2) and σ_B (from term 3) are:

$$\sigma_A = \sqrt{\frac{1}{N-2}\sum_{i=1}^{N}\left(A_{curve-fit}(T_i) - A_{i,measured}\right)^2 + \left(\frac{\partial A}{\partial T}\Delta T\right)^2}, \tag{A.6}$$

$$\sigma_B = \sqrt{\frac{1}{N-2}\sum_{i=1}^{N}\left(B_{curve-fit}(T_i) - B_{i,measured}\right)^2 + \left(\frac{\partial B}{\partial T}\Delta T\right)^2}. \tag{A.7}$$

In both these equations, the first term represents the uncertainty from the curve-fit and the second term represents the uncertainty due to the maximum variation of the jet temperature (ΔT = 1.2 °C) for one King's Law calibration.

Given the above, the relative standard uncertainty is found to be 1.3 %.

DAQ board resolution

The resolution uncertainty of the data acquisition board is random and assumed to have a uniform distribution. The following expression is used to calculate the relative standard uncertainty (Jørgensen, 2002):

$$uncertainty = \left(\frac{1}{\sqrt{3}} \frac{1}{U} \frac{\partial U}{\partial E} \frac{E_{DAQ}}{2^n} \right) \times 100\%, \tag{A.8}$$

where $\partial U / \partial E$ is the slope of the calibration curve (largest value is 31.4), E_{DAQ} is the voltage span used to acquire the data (10 V) and n is the number of bits (16) of the acquisition system. The relative standard uncertainty is 0.015 %.

Temperature measurements

Since the velocity measurements depend on the cold-wire measurements (to correct A and B), the uncertainties in cold-wire temperature measurements are accounted for by incorporating the uncertainties presented in sub-section A.1.1. The value used is 0.33% which is half of the total uncertainty calculated in sub-section A.1.1 to be able to add all the uncertainties together in quadrature before achieving a confidence level of 95 %.

Ambient pressure and humidity variations

Changes in ambient pressure and humidity are assumed to add negligible uncertainty to the velocity measurements. (The largest observed change in pressure was 1.3 kPa (10 mm Hg) and the experiments were performed during winter when the relative humidity in the laboratory was less than 35 %.)

Probe positioning

Errors due to probe positioning were accounted for (as mentioned in section 4.1) by correcting the effective angle by 1.5°. Any remaining uncertainty is assumed to be negligible on the velocity measurements.

Total expanded uncertainty for the velocity measurements

All the uncertainties are summarized in the table A.2 in order of decreasing importance.

Sources of error	Relative standard uncertainty
Calibration curve-fit	1.3 %
Calibration equipment	1 %
Temperature measurements	0.33 %
DAQ board resolution	0.015 %
Anemometer	negligible
Ambient pressure and humidity variations	negligible
Probe positioning	negligible

Table A.2: The uncertainties in the velocity measurements

The overall expanded uncertainty is calculated from equation A.4. Therefore, substituting the values of table A.2 into this equation results in a total expanded uncertainty of **3.3%**.

A.1.3 Uncertainty in Pr_T and r

The uncertainty in Pr_T consists of combining the uncertainties in each term used to calculate Pr_T. Before proceeding, note that the uncertainties obtained in sections A.1.1 and A.1.2 for the instantaneous measurements of velocity and temperature will be used for both the mean and fluctuating components as well. In other words:

$$\frac{\delta\widetilde{U}}{\widetilde{U}} = \frac{\delta\overline{U}}{\overline{U}} = \frac{\delta u}{u} = \frac{\delta\widetilde{V}}{\widetilde{V}} = \frac{\delta\overline{V}}{\overline{V}} = \frac{\delta v}{v}, \tag{A.9}$$

and similarly for the temperature values. Hence, for $\overline{uv}$ and $\overline{v\theta}$, the relative uncertainties are directly calculated by the propagation of uncertainties as follows:

$$\frac{\delta\overline{uv}}{\overline{uv}} = \sqrt{\left(\frac{\delta u}{u}\right)^2 + \left(\frac{\delta v}{v}\right)^2} = \sqrt{2\times(3.3\%)^2} = 4.7\%, \tag{A.10}$$

$$\frac{\delta\overline{v\theta}}{\overline{v\theta}} = \sqrt{\left(\frac{\delta v}{v}\right)^2 + \left(\frac{\delta\theta}{\theta}\right)^2} = \sqrt{(3.3\%)^2 + (0.65\%)^2} = 3.4\%. \tag{A.11}$$

For $\partial\overline{U}/\partial y$, the relative uncertainty is computed from both the curve-fits to the mean velocity profile, and from the uncertainty of the mean velocity measurements. The relative uncertainty due to the mean velocity's curve-fit is computed in a similar manner as presented in sections A.1.1 and A.1.2 for other curve-fits. Using the curve-fit for the mean velocity profile:

$$\frac{\delta(\overline{U}_{fit})}{\overline{U}_{fit}} = 2\sqrt{\left(\frac{1}{N-4}\sum_{i=1}^{N}\left(\frac{\overline{U}_{curve-fit}((y/D)_i) - \overline{U}_{i,measured}}{\overline{U}_{curve-fit}((y/D)_i)}\right)^2\right)} = 0.7\%. \tag{A.12}$$

Thus, the relative uncertainty for $\partial\overline{U}/\partial y$ becomes:

$$\frac{\delta(\partial\overline{U}/\partial y)}{\partial\overline{U}/\partial y} = \sqrt{\left(\frac{\delta(\overline{U}_{fit})}{\overline{U}_{fit}}\right)^2 + \left(\frac{\delta\overline{U}}{\overline{U}}\right)^2} = \sqrt{(0.7\%)^2 + (3.3\%)^2} = 3.4\%. \tag{A.13}$$

Likewise, the same procedure can be repeated to compute the relative uncertainty from the curve-fit to the mean temperature excess used to calculate $\partial\overline{T}/\partial y$. For the case of the flow heated by the cylinder:

$$\frac{\delta(\overline{\Delta T}_{fit})}{\overline{\Delta T}_{fit}} = 2\sqrt{\left(\frac{1}{N-5}\sum_{i=1}^{N}\left(\frac{\overline{\Delta T}_{curve-fit}((y/D)_i) - \overline{\Delta T}_{i,measured}}{\overline{\Delta T}_{curve-fit}((y/D)_i)}\right)^2\right)} = 9.2\%, \tag{A.14}$$

and 11.2% for the case of the mandoline.

Additionally, to remove the effect of thermal drift which can occur over the course of an experiment, the free-stream temperature is recorded using a thermocouple to obtain the mean temperature excess. However, the mean temperature

excess measurements have a higher uncertainty than the fluctuating part because of the inaccuracies in estimating the free-stream temperature. Hence, for each experiment the mean temperature excess profile is measured four times. The average of these four passes is then computed. Averaging the four passes reduces the overall relative standard uncertainty (calculated from a standard deviation of at most 0.05°C in the mean temperature excess) from 5.8% to 3%. For a 95% confidence level, the relative uncertainty of measuring the mean temperature excess is 6%.

Combining all sources of relative uncertainty for $\partial\overline{T}/\partial y$ results in the following for the case of the heated cylinder:

$$\frac{\delta(\partial\overline{T}/\partial y)}{\partial\overline{T}/\partial y} = \sqrt{\left(\frac{\delta(\overline{\Delta T}_{fit})}{\overline{\Delta T}_{fit}}\right)^2 + \left(\frac{\delta\overline{T}}{\overline{T}}\right)^2 + \left(\frac{\delta\overline{\Delta T}}{\overline{\Delta T}}\right)^2} = \sqrt{(9.2\%)^2 + (0.65\%)^2 + (6\%)^2} = 11\% \tag{A.15}$$

and 12.7% for the case of the flow heated by the mandoline.

Finally, to obtain the total relative uncertainty in Pr_T, the propagation of uncertainties is again applied:

$$\left[\frac{\delta(\mathrm{Pr}_T)}{\mathrm{Pr}_T}\right]_{cylinder} = \sqrt{\left(\frac{\delta\overline{uv}}{\overline{uv}}\right)^2 + \left(\frac{\delta\overline{v\theta}}{\overline{v\theta}}\right)^2 + \left(\frac{\delta(\partial\overline{U}/\partial y)}{\partial\overline{U}/\partial y}\right)^2 + \left(\frac{\delta(\partial\overline{T}/\partial y)}{\partial\overline{T}/\partial y}\right)^2} = 13\%, \tag{A.16}$$

$$\left[\frac{\delta(\mathrm{Pr}_T)}{\mathrm{Pr}_T}\right]_{mandoline} = \sqrt{\left(\frac{\delta\overline{uv}}{\overline{uv}}\right)^2 + \left(\frac{\delta\overline{v\theta}}{\overline{v\theta}}\right)^2 + \left(\frac{\delta(\partial\overline{U}/\partial y)}{\partial\overline{U}/\partial y}\right)^2 + \left(\frac{\delta(\partial\overline{T}/\partial y)}{\partial\overline{T}/\partial y}\right)^2} = 14\%. \tag{A.17}$$

However, since the values of Pr_T on both sides of the wake were averaged, the uncertainty should accordingly be reduced. Strictly, the absolute uncertainty of each

Pr_T should be computed and the weighted average of the two Pr_T values obtained (Taylor, 1997). However, taking the arithmetic mean of the two values, and using the relative uncertainties should provide a sufficient estimate of the overall error in the Pr_T measurements. Thus, the relative uncertainty in Pr_T is reduced to 9.2% for the cylinder and 9.9% for the mandoline (figure A.1).

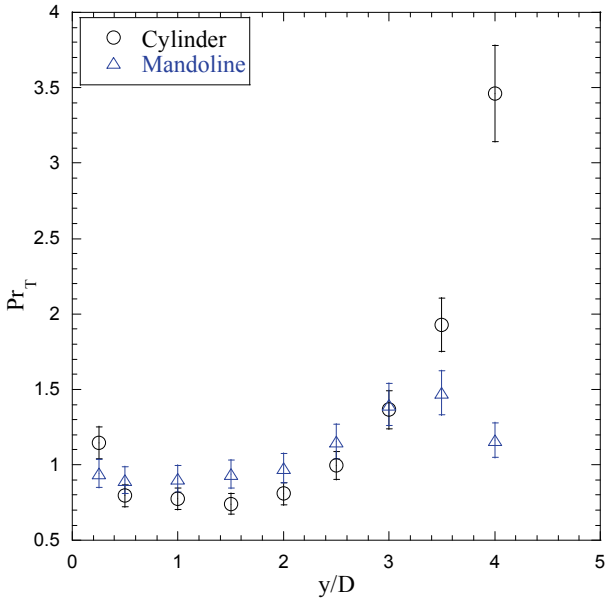

Figure A.1: Turbulent Prandtl number distribution with error bars

Similarly, the same procedure used to obtain the uncertainties for the Pr_T measurements can be applied to obtain the uncertainties in the *r* measurements. The total relative uncertainty for *r* is 9.4% (figure A.2).

The uncertainties presented here demonstrate that the exact quantitative values of Pr_T and *r* may fall within a small region around the reported values. However, even in the most extreme cases, the qualitative conclusions remain the same: (i) the values of Pr_T and *r* vary across the wake, (ii) their average values are

not always near the ones chosen by modellers, and most importantly (iii) the two scalar field initial conditions resulted in different values of Pr_T and r.

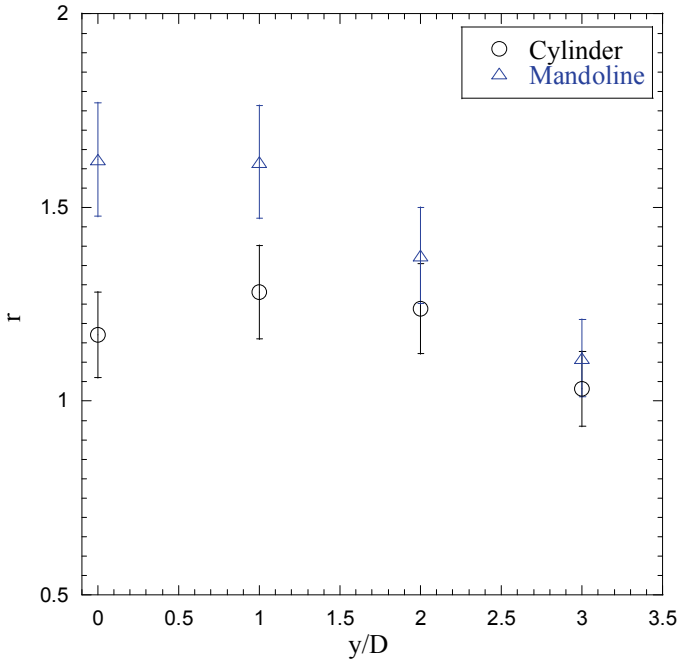

Figure A.2: Mechanical-to-thermal time-scale ratio distribution with error bars